Original Article | **Open Access**

Extracellular Vesicles and Circulating Nucleic Acids

Raboshakga *et al. Extracell Vesicles Circ Nucleic Acids.* 2026;7:1980-2005 **DOI:**10.20517/evcna.2026.138

PSMA-targeted extracellular vesicles deliver siADAM9 to suppress tumor progression and enhance androgen-targeted therapy in prostate cancer

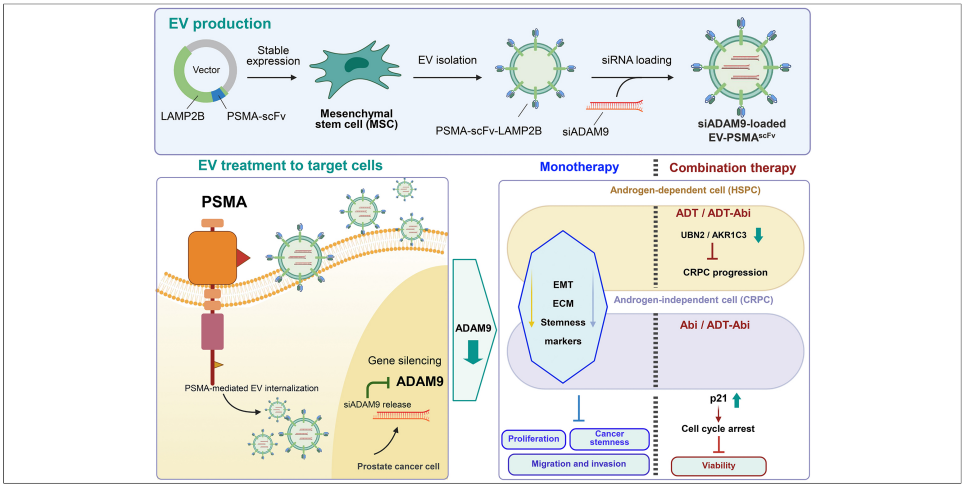
Mafewu Olga Raboshakga[1], Anh Duy Do[2], Gwo Harn Max Shiau[3,4], Katsumi Shigemura[5], Chia-Ling Hsieh[4,6], Shian-Ying Sung[1,4,7,8]

Keywords:
Extracellular vesicles, prostate cancer, ADAM9, siRNA delivery, PSMA-targeted therapy, therapeutic resistance

Citation: Raboshakga MO, Do AD, Shiau GHM, Shigemura K, Hsieh CL, Sung SY. PSMA-targeted extracellular vesicles deliver siADAM9 to suppress tumor progression and enhance androgen-targeted therapy in prostate cancer. *Extracell Vesicles Circ Nucleic Acids.* 2026;7:1980-2005. https://dx.doi.org/10.20517/evcna.2026.138

Received: 2 Jul 2026 **First Decision:** 3 Aug 2026 **Revised:** 12 Oct 2026 **Accepted:** 12 Oct 2026 **Published:** 2 Nov 2026

Academic Editor: Yoke Peng Loh
Copy Editor: Ting-Ting Hu
Production Editor: Ting-Ting Hu



Abstract

Aim: The progression of prostate cancer to metastatic and castration-resistant disease remains a major therapeutic challenge, and a disintegrin and metalloproteinase 9 (ADAM9) has emerged as a key regulator of tumor progression and adaptive androgen receptor signaling. We aimed to develop a prostate-specific membrane antigen (PSMA)-targeted extracellular vesicle (EV) platform for selective delivery of small interfering RNA (siRNA) against ADAM9 (siADAM9) and evaluate its therapeutic potential in prostate cancer.

Methods: Mesenchymal stem cell (MSC)-derived EVs were engineered to display a PSMA-targeting single-chain variable fragment (PSMA-scFv). Targeting specificity and cellular uptake were evaluated in PSMA-expressing and PSMA-negative prostate cancer cells. Functional effects of EV-mediated siADAM9 delivery were assessed by proliferation,

[1]International Ph.D. Program for Translational Science, College of Medical Science and Technology, Taipei Medical University, Taipei 11031, Taiwan.
[2]Department of Physiology, Pathophysiology and Immunology, Pham Ngoc Thach University of Medicine, Ho Chi Minh City 700000, Vietnam.
[3]Institute of Biomedical Sciences, Academia Sinica, Taipei 115, Taiwan.
[4]The Ph.D. Program for Translational Medicine, College of Medical Science and Technology, Taipei Medical University, Taipei 11031, Taiwan.
[5]Department of Urology, Kurashiki Medical Center, Kurashiki 710-8522, Japan.
[6]General Clinical Research Center, Chung Shan Medical University Hospital, Taichung 40201, Taiwan.

[7]Department of Medical Research, Chung Shan Medical University Hospital, Taichung 40201, Taiwan.
[8]Institute of Medicine, Chung Shan Medical University, Taichung 40201, Taiwan.

Correspondence to: Dr. Shian-Ying Sung, Institute of Medicine, Chung Shan Medical University, Taichung 40201, Taiwan. E-mail: ssung@csmu.edu.tw; Dr. Chia-Ling Hsieh, General Clinical Research Center, Chung Shan Medical University Hospital, Taichung 40201, Taiwan. E-mail: cshe1539@csh.org.tw

migration, and sphere formation assays in hormone-sensitive (LNCaP) and castration-resistant (CWR22Rv1) prostate cancer models. Gene and protein expression were analyzed by reverse transcription quantitative polymerase chain reaction (RT-qPCR) and immunoblotting. Therapeutic efficacy was further evaluated in combination with androgen deprivation therapy and abiraterone.

Results: PSMA-scFv functionalization enabled selective EV binding and uptake in a PSMA-dependent manner. Through this targeting strategy, EV-mediated siADAM9 delivery effectively suppressed ADAM9 expression and inhibited malignant phenotypes, including proliferation, migration, and tumor sphere formation, while reversing epithelial-mesenchymal transition- and stemness-associated molecular programs. Moreover, EVs loaded with siADAM9 (EV-siADAM9) enhanced the efficacy of androgen-targeted therapy in both hormone-sensitive and castration-resistant prostate cancer models. These effects were associated with disruption of ADAM9 downstream signaling, including aldo-keto reductase family 1 member C3 (AKR1C3)-mediated androgen biosynthesis and cell-cycle regulation.

Conclusion: These findings provide *in vitro* proof-of-concept that PSMA-targeted EVs preferentially deliver siADAM9, suppress tumor-promoting programs, and enhance androgen-targeted therapy, supporting further preclinical evaluation of this platform.

INTRODUCTION

Androgen deprivation therapy (ADT) remains the standard treatment for hormone-sensitive prostate cancer (HSPC); however, the majority of patients ultimately develop resistance and progress to castration-resistant prostate cancer (CRPC), a lethal disease state with limited therapeutic options[1]. Increasing evidence indicates that resistance is not solely acquired but may arise from pre-existing tumor subpopulations with adaptive molecular programs[2], highlighting the need for therapeutic strategies that target both early resistance mechanisms and advanced disease progression. A central feature of CRPC development is the restoration of androgen receptor (AR) signaling under androgen-deprived conditions. This process is frequently mediated by adaptive steroidogenic reprogramming, enabling sustained intratumoral androgen synthesis[3]. Targeting upstream regulators of this adaptive steroidogenic reprogramming may therefore provide a more durable therapeutic approach than direct AR inhibition alone.

Among candidate regulators, a disintegrin and metalloproteinase 9 (ADAM9) has emerged as a critical mediator of prostate cancer progression and therapeutic resistance. ADAM9 is overexpressed in prostate cancer compared with benign prostate tissue, and elevated tumor ADAM9 expression has been associated with shorter prostate-specific antigen (PSA) relapse-free survival following radical prostatectomy, supporting its clinical relevance as a prognostic marker[4]. ADAM9 expression is significantly upregulated during the transition to androgen-independent and metastatic states and is induced under tumor stress conditions, including oxidative stress and hypoxia[5]. Functionally, ADAM9 has been implicated in resistance to radiation and chemotherapy and in prostate cancer growth and metastatic progression[6]. Mechanistically, ADAM9 promotes resistance to androgen deprivation through activation of ubinuclein 2 (UBN2)/aldo-keto reductase family 1 member C3 (AKR1C3) axis, which facilitates intracrine androgen biosynthesis and supports androgen-independent tumor survival[7]. These findings position ADAM9 as a central mediator linking tumor microenvironment signaling, adaptive survival pathways, and steroidogenic reprogramming, making it an attractive therapeutic target across both hormone-sensitive and castration-resistant disease states.

RNA interference-based therapeutics, particularly small interfering RNA (siRNA), offer a highly specific strategy for silencing oncogenic drivers such as ADAM9; however, their clinical translation is limited by poor systemic stability, rapid nuclease degradation, inefficient intracellular delivery, and non-specific biodistribution[8]. These limitations remain a major barrier to effective RNA-based cancer therapy. Extracellular vesicles (EVs) have recently emerged as promising endogenous nanocarriers for nucleic acid therapeutics. These vesicles naturally mediate intercellular communication through the transfer of functional RNA cargo and provide intrinsic protection against enzymatic degradation while facilitating cellular uptake via membrane fusion or endocytosis. Owing to these properties, EVs are increasingly explored as biologically derived delivery systems for precision RNA therapeutics[9]. Mesenchymal stem cell (MSC)-derived EVs are widely used as a scalable and biocompatible source of EVs for RNA delivery, and have been extensively explored as reproducible platforms for therapeutic engineering. Accumulating evidence, including our previous work, has demonstrated that MSC-EVs can effectively deliver therapeutic RNA molecules and suppress tumor progression, supporting their translational potential. Notably, a first-in-human clinical trial evaluating MSC-derived EVs loaded with KRASG12D-targeting siRNA in metastatic pancreatic cancer (ClinicalTrials.gov identifier: NCT03608631) is currently ongoing, further supporting EV-based siRNA delivery as a promising strategy for precision cancer therapy.

Despite these advantages, native EVs exhibit limited targeting specificity, resulting in non-selective biodistribution and reduced therapeutic efficiency. Active targeting strategies are therefore required to enhance tumor selectivity. Prostate-specific membrane antigen (PSMA), also known as folate hydrolase 1 (FOLH1), is a well-established surface biomarker that is highly expressed in advanced prostate cancer and correlates with tumor aggressiveness and metastatic potential[10]. Monoclonal antibodies targeting the extracellular domain of PSMA, including J591-based constructs, have demonstrated clinical applicability in both imaging and therapeutic settings[11]. While full-length antibodies provide prolonged circulation and stable antigen binding, their large size and fragment crystallizable (Fc)-mediated interactions may limit their suitability for nanoscale surface engineering applications. In contrast, antibody fragments such as single-chain variable fragments (scFvs) retain antigen specificity while offering reduced steric hindrance and improved tissue penetration[12]. Recent studies have demonstrated the feasibility of engineering PSMA-targeted exosome-like nanovesicles for enhanced tumor targeting[13]. However, these approaches primarily focus on delivery efficiency and targeting capability, with limited investigation into modulation of key oncogenic resistance pathways or integration with clinically relevant therapeutic regimens.

In this study, we engineered MSC-derived EVs displaying PSMA-targeting scFvs and loaded with siRNA targeting ADAM9. We conducted an *in vitro* proof-of-concept evaluation of this platform to determine whether PSMA functionalization could provide PSMA-dependent enhancement of EV delivery and whether EV-mediated ADAM9 silencing could suppress tumor-promoting programs associated with therapeutic resistance. We further evaluated its therapeutic potential in both hormone-sensitive and CRPC models, including combination with ADT and abiraterone, to assess its capacity to suppress steroidogenic compensation and improve treatment durability.

METHODS

Study design

This study was designed as an *in vitro* proof-of-concept investigation to evaluate the efficacy of PSMA-targeted EVs for the delivery of ADAM9-targeting siRNA and to investigate their effects on prostate cancer cell growth, migration, and resistance-associated signaling. Experiments were conducted using both

hormone-sensitive and CRPC cell models. Functional assays, molecular analyses, and EV characterization were performed to assess delivery efficiency and biological effects.

Cell lines and culture conditions

Human prostate cancer cell lines LNCaP [CRL-1740; research resource identifier (RRID): CVCL_0395], CWR22Rv1 (CRL-2505; RRID:CVCL_1045), PC3 (CRL-1435; RRID:CVCL_0035), DU145 (HTB-81; RRID:CVCL_0105), and C4-2 (CRL-3314; RRID:CVCL_4782) were obtained from the American Type Culture Collection (ATCC, Manassas, USA) and maintained in Roswell Park Memorial Institute medium (RPMI-1640). A reference short tandem repeat (STR) profile is available via the ATCC STR database; no additional STR profiling was performed in our laboratory for this study. An immortalized human bone marrow-derived MSC line, previously established and kindly provided by Dr. Shih-Chieh Hung[14], was cultured in low-glucose Dulbecco's Modified Eagle Medium (DMEM). HEK293FT and HEK293A cells (Invitrogen, Waltham, USA) were maintained in high-glucose DMEM. All media were supplemented with 10% fetal bovine serum (FBS) and 1% penicillin-streptomycin-neomycin unless otherwise specified. Androgen-targeted therapy was carried out by culturing prostate cancer cells in phenol red-free RPMI-1640 with 5% charcoal-stripped serum (CSS) to eliminate exogenous steroid hormones and/or treating them with 10 μM abiraterone (Cat. #SML1527, Sigma-Aldrich, St. Louis, USA) to inhibit endogenous androgen synthesis. For sphere formation, cells were cultured in DMEM/F12 (1:1) supplemented with B27 (Cat. #17504044, ThermoFisher Scientific, Waltham, USA), 20 ng/mL basic fibroblast growth factor (Cat. #3718-FB, R&D Systems, Minneapolis, USA), and 20 ng/mL epidermal growth factor (Cat. #236-EG, R&D Systems, Minneapolis, USA). Unless otherwise specified, all media and reagents were obtained from Cytiva (Marlborough, USA). All cell lines were routinely tested for mycoplasma contamination using a Mycoplasma polymerase chain reaction (PCR) detection kit (Cat. #G238, Applied Biological Materials, Richmond, BC, Canada), and were generally used within approximately 30 passages of receipt.

Construction of PSMA-scFv-LAMP2B lentiviral expression vector

A pUC57 plasmid encoding a PSMA-targeting scFv (PSMA-scFv) was constructed by Genomics BioSci & Tech (New Taipei City, Taiwan) using the variable regions of the J591 antibody (GenBank: FR853148.1 and FR853149.1) linked by a $(Gly_4Ser)_3$ peptide linker. The PSMA-scFv cassette was cloned into a lysosome-associated membrane protein 2B (LAMP2B) expression vector (Cat. #RC200456; OriGene, Rockville, USA) to enable EV surface display. For initial validation of the fusion construct, the PSMA-scFv-LAMP2B plasmid was transiently transfected into HEK293A cells using Maestrofectin Transfection Reagent (Cat. #MF002; Omics Bio, Taipei, Taiwan) according to the manufacturer's protocol. Following validation, the PSMA-scFv-LAMP2B fusion construct was subsequently subcloned into a lentiviral vector (pLAS3w.Pbsd) using an In-Fusion Snap Assembly Kit (Cat. #638947; Takara Bio, Kusatsu, Japan) according to the manufacturer's instructions. A LAMP2B-only lentiviral construct was generated in parallel as a control.

Generation of engineered cell lines

The PSMA-scFv-LAMP2B and LAMP2B-only lentiviral constructs were used to generate engineered MSCs for EV production. In parallel, a lentiviral vector encoding human FOLH1 (Cat. #20736061; Applied Biological Materials, Richmond, Canada) was used to establish PSMA-expressing prostate cancer cell models. Lentiviral particles were produced by transfecting HEK293FT cells using Maestrofectin. Viral supernatants were collected and used to transduce target cells to establish stable cell lines following protocols provided by the RNAi Core Facility (Academia Sinica, Taipei, Taiwan).

EV collection and isolation

EVs were isolated from conditioned media of parental and engineered MSCs cultured in serum-free conditions for 48 h. The media were filtered through a 0.22 μm pore-size membrane filter (Cat. #SLGVR33RS; Merck Millipore, Burlington, MA, USA), and subsequently concentrated using Vivaspin

concentrators (Cat. #VS15T12, Sartorius, Göttingen, Germany). EVs were isolated from the media using the ExoEasy Maxi kit, according to the manufacturer's protocol (Cat. #76064, Qiagen, Hilden, Germany), followed by buffer exchange to phosphate-buffered saline (PBS) using Vivaspin (Cat. #VS04T9, Sartorius, Göttingen, Germany) centrifugal units.

Nanoparticle tracking analysis (NTA)

EV size distribution and particle concentration were analyzed using a NanoSight NS300 system (Malvern Panalytical, Malvern, UK). EV samples were diluted in PBS to achieve a particle concentration within the optimal detection range (1×10^7-1×10^9 particles/mL). For each sample, three 60-s videos were captured at camera level 13 and detection threshold 5 under constant temperature control (25 °C). Mean particle size and concentration (particles/mL) were determined from three independent measurements.

Transmission electron microscopy (TEM)

Morphology and structural features of EVs were assessed by TEM. A small volume of EV suspension (10 μL) was applied onto a formvar/carbon-coated TEM grid and allowed to adsorb for 2 min. Excess liquid was carefully removed using filter paper. The grid was then stained by adding 10 μL of 2% uranyl acetate solution for 1 min. After removing excess stain with filter paper, the grid was air-dried for 10 min prior to imaging under HT-7700 TEM (Hitachi High-Technologies, Tokyo, Japan).

siRNA loading into EVs

siRNAs targeting ADAM9 (siADAM9 #1 and #2), PSMA-targeting siRNA (siPSMA), and negative control siRNA (siNC) were chemically synthesized (sequences provided in Supplementary Table 1) by GenePharma (Shanghai, China). siRNAs (10 μM, 1.204×10^{11} molecules per 1 μL) were loaded into EVs using the Exo-Fect siRNA/miRNA Transfection Kit (Cat. #EXFT200A-1; System Biosciences, Palo Alto, USA), according to the manufacturer's instructions. To eliminate residual unencapsulated siRNA, the reaction mixture was treated with ribonuclease (RNase) at 37 °C for 1 h, and then subjected to EVs isolation as prescribed, and used for subsequent assays.

Quantification of encapsulated siRNA

Total RNA was extracted from EVs using the Total Exosome RNA and Protein Isolation Kit (Thermo Fisher Scientific, Waltham, USA) according to the manufacturer's instructions. The quantity of encapsulated siRNA was determined by reverse transcription quantitative polymerase chain reaction (RT-qPCR) (primer information shown in Supplementary Table 2) using a standard curve generated from serially diluted synthetic siRNA standards. The absolute copy number of siRNA was calculated based on the standard curve, and normalized to EV particle numbers determined by NTA.

Flow cytometry analysis

Flow cytometric data were acquired using a BD FACS Canto II flow cytometer (BD Biosciences, New Jersey, USA) and analyzed with FlowJo software (version 10.8.1) (FlowJo, LLC, Ashland, USA). Appropriate gating strategies were applied to exclude debris and doublets.

Surface PSMA expression

Surface expression of PSMA was assessed by flow cytometry. Cell suspensions were incubated with an anti-PSMA primary antibody (1 μg/mL; Cat. #GTKUX80149, GenTex, Irvine, USA) or an isotype-matched immunoglobulin G (IgG) control (0.5 μg/mL; Cat. #MBAB002; R&D Systems, Minneapolis, USA), followed by incubation with an Alexa Fluor 488-conjugated anti-mouse IgG secondary antibody (2 μg/mL; Cat. #A21202, Invitrogen, Thermo Fisher Scientific). After washing to remove unbound antibodies, cells were subjected to flow cytometric analysis.

Protein-L binding analysis

To evaluate surface display of scFv-engineered EVs, flow cytometric analysis was performed using the Exosome-Human CD63 Isolation/Detection Reagent (Cat. #10606D, Thermo Fisher Scientific), following the manufacturer's protocol with minor modifications. Briefly, EVs were captured using CD63 antibody-coated Dynabeads and washed with isolation buffer [PBS containing 0.1% bovine serum albumin (BSA)]. Bead-bound EVs were incubated with phycoerythrin (PE)-labeled recombinant Protein L (Cat. #RPL-PP2H2; ACRO Biosystems, Newark, USA) at room temperature for 30 min to detect scFv binding. Following incubation, samples were washed, magnetically separated to remove unbound reagents, and resuspended in isolation buffer for analysis.

EV treatment of prostate cancer cells

Unless otherwise specified, prostate cancer cells were treated with EVs at a standardized EV-to-cell ratio of 1×10^4 particles per cell in all cellular experiments. EV particle numbers were determined by NTA before treatment. For siRNA-loaded EVs, the corresponding siRNA dose was estimated based on the experimentally determined siRNA loading per EV. Treatment duration and frequency are specified for each individual assay.

EV binding to prostate cancer cells

Parental, LAMP2B, or PSMA^{scFv} EVs were fluorescently labeled using ExoGlow (Cat. #EXOGP100A-1, System Biosciences) or ExoSparkler (Cat. #EX02; Dojindo Laboratories, Kumamoto, Japan) membrane-labeling kits according to the manufacturer's instructions. Approximately 5×10^{10} EV particles were used for each labeling reaction. Following labeling, free dye was removed, and the labeled EVs were washed and resuspended in PBS. EV particle concentrations were subsequently re-determined by NTA before use. Labeled EVs (1×10^9 particles) were incubated with 1×10^5 prostate cancer cells for 1 h at room temperature in the dark. After washing to remove unbound EVs, cells were subjected to flow cytometric analysis. EV binding was quantified using FlowJo software based on the fluorescence intensity of cell-associated labeled EVs.

Confocal microscopic assay

LNCaP (1.5×10^5) and PC3 (2.5×10^5) were seeded on glass coverslips and incubated overnight. Cells were stained with CellBrite Cytoplasmic Membrane Dye (Cat. #30021; Biotium, Fremont, USA), according to the manufacturer's instructions, followed by incubation with fluorescently labeled parental, LAMP2B, or PSMA^{scFv} EVs. After washing, cells were fixed with 4% paraformaldehyde and mounted with 4',6-diamidino-2-phenylindole (DAPI)-containing medium (Cat. #sc-24941; Santa Cruz Biotechnology, Dallas, USA). Images were acquired using a Stellaris confocal microscope (Leica Microsystems, Wetzlar, Germany). EV-associated fluorescence intensity was quantified using Fiji/ImageJ software. Three to four fields of view were analyzed per sample, and fluorescence intensities were quantified and averaged for comparison among EV treatment groups. For assessment of intracellular localization, confocal z-stack images were acquired and reconstructed to generate orthogonal views, allowing EV-associated fluorescence to be evaluated relative to the membrane-defined cellular boundaries.

Western blot analysis

Protein extracts from cells and EVs were prepared and separated by sodium dodecyl sulfate-polyacrylamide gel electrophoresis (SDS-PAGE). Proteins were transferred onto membranes, which were subsequently blocked and incubated with primary antibodies (typically 1:1,000 dilution) at 4 °C overnight. Membranes were then incubated with appropriate horseradish peroxidase-conjugated secondary antibodies (1:10,000 dilution). Protein bands were detected using an enhanced chemiluminescence detection kit (Cat. # JT96-K002, T-Pro Biotechnology) and imaged using an Amersham Imager 600 system (Cytiva, Marlborough, USA). Detailed information on primary antibodies is provided in Supplementary Table 3.

Reverse transcription quantitative polymerase chain reaction (RT-qPCR) analysis

Total RNA was extracted from cells using NC RNA extraction reagent (Cat. #MRE-N3200; EBL Biotechnology, Taipei, Taiwan) according to the manufacturer's instructions. Complementary DNA (cDNA) was synthesized from total RNA using the PrimeScript RT reagent kit (Cat. # RR037A, Takara Bio). Quantitative PCR was performed using gene-specific primers (listed in Supplementary Table 4) and the QuantiNova SYBR Green PCR kit (Cat. # 208052, Qiagen) on a LightCycler 96 system (Roche, Basel, Switzerland), following the manufacturers' protocols. Relative gene expression levels were calculated using the $2^{-\Delta\Delta Ct}$ method, with HSPCB serving as the internal reference gene for normalization.

Transwell migration assay

Cell migration was assessed using 8-μm pores Transwell inserts (Cat. #MCEP24H48, Merck Millipore), with three biological replicates per condition. The lower chamber was filled with 800 μL of RPMI-1640 supplemented with 1% FBS to serve as a chemoattractant. EV-treated cells (5×10^4) suspended in a 200 μL serum-free medium were seeded into the upper chambers and incubated under standard culture conditions. Following incubation, non-migrated cells on the upper surface of the membrane were removed. Cells that had migrated to the lower surface were fixed with 10% neutral-buffered formalin, stained with crystal violet for 30 min at room temperature, and rinsed with distilled water to remove excess stain. Membranes were air-dried, and migrated cells were imaged in randomly selected fields using a light microscope. For quantitative analysis, retained crystal violet was solubilized in a solution containing distilled water, ethanol, and acetic acid (1:1:2, v/v/v). Absorbance was measured at 590 nm using a microplate reader, and cell migration was quantified based on the absorbance of solubilized crystal violet.

Wound healing assay

EV-treated cells were seeded into culture insert compartments (Cat. # 80466, Ibidi, Gräfelfing, Germany) at densities of 2.5×10^4 cells/100 μL and maintained under standard culture conditions. After cell attachment, inserts were removed to generate a defined cell-free gap, and wells were gently washed with PBS to remove unattached cells. The resulting cell-free gap or wound area was imaged at 0, 24, and 48 h microscopically. The wound area at each time point was quantified using ImageJ software (National Institutes of Health, USA), and wound closure at 24 and 48 h was calculated relative to the initial wound area at 0.

Cell proliferation assay

Cell proliferation was assessed using a WST-8 assay. EV-treated cells were seeded at a density of 5×10^3 cells per well in 96-well plates and incubated overnight under standard culture conditions. At the indicated time points, 10 μL of WST-8 reagent (Cat. #11644807001; Roche, Basel, Switzerland) was added to each well, followed by incubation for 4 h. Absorbance was measured at 440/630 nm using a microplate reader (CLARIOstar Plus, BMG Labtech, Ortenberg, Germany).

Sphere formation assay

Sphere formation assay was performed under non-adherent conditions using serum-free sphere-forming medium. EV-treated cells were seeded at a density of 2.5×10^3 cells per well in ultra-low attachment plates and maintained in suspension culture from day 0. EV-siADAM9 treatment was initiated on day 3 and repeated every 3 days thereafter to ensure continuous exposure over 7-14 days. At the endpoint, spheres were imaged for assessment of number and size, and subsequently collected for downstream RNA and protein analyses.

Statistical analysis

Unless otherwise specified, experiments were performed in triplicate and repeated independently at least three times. Data are presented as mean ± standard error of the mean (SEM) unless otherwise stated. Statistical analyses were conducted using GraphPad Prism software (GraphPad, San Diego, CA, USA).

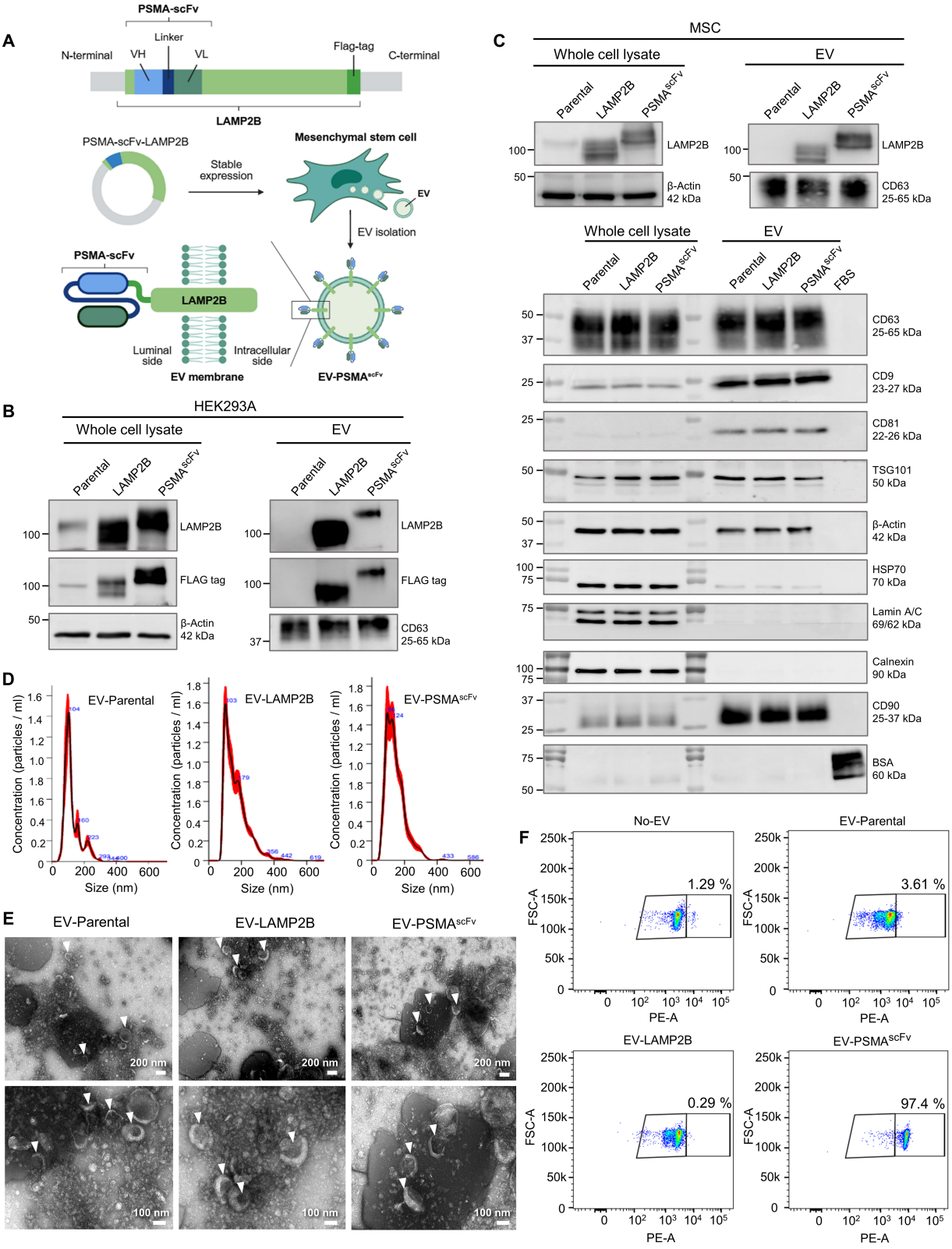


Figure 1. Genetic modification and characterization of PSMA-scFv MSC-EVs. (A) Schematic representation of EV genetic modification. The VH and VL domains of the J591 monoclonal antibody were linked by a peptide linker to generate the PSMA-scFv. The construct was fused to LAMP2B and expressed in HEK293A and BM-MSC cells to generate PSMA-scFv displaying EVs; (B and C) Expression of PSMA-scFv in engineered HEK293A and MSC cells and characterization of the corresponding EVs. Western blot analysis showing PSMA-scFv expression in WCL of HEK293A (B) and MSCs (C) and in their respective EV fractions, detected using LAMP2B and FLAG antibodies. Blots were normalized to β-actin for WCL and CD63 for EV fractions. EV marker analysis of Parental, LAMP2B, and PSMA-scFv MSC-derived EVs confirmed the presence of canonical EV markers in accordance with MISEV 2023 guidelines (C); (D) NTA of MSC-EVs. Representative NTA plots showing particle size distribution and concentration of PSMA^{scFv}-engineered MSC-EVs, compared to Parental and LAMP2B EVs; (E) TEM. Micrographs illustrating the morphology and size of genetically modified MSC-EVs (LAMP2B and PSMA-scFv) and unmodified (Parental). White arrows indicate EV particles. Scale bars: 200 nm (top) and 100 nm (bottom); (F) Surface

localization of PSMA-scFv on MSC-EVs. Flow-cytometric analysis following conjugation with Protein L and CD63 magnetic beads, demonstrating the external topology of PSMA-ScFv on the EVs surface. Representative dot plots show protein L-binding profiles for Parental, LAMP2B, and PSMA-scFv MSC-EVs. Three independent EV preparations were analyzed (n = 3). Representative NTA, TEM, and Protein L images are shown, with each analysis performed in triplicate. Immunoblot analyses were performed using three independent biological repeats (n = 3). EVs: Extracellular vesicles; PSMA: prostate-specific membrane antigen; scFv: single-chain variable fragment; MSCs: mesenchymal stem cells; BM-MSC: bone marrow-derived mesenchymal stem cell; LAMP2B: lysosome-associated membrane protein 2B; VH: variable heavy; VL: variable light; WCL: whole-cell lysate; MISEV: Minimal Information for Studies of Extracellular Vesicles; NTA: nanoparticle tracking analysis; TEM: transmission electron microscopy; PE: phycoerythrin; CD9: cluster of differentiation 9; CD63: cluster of differentiation 63; CD81: cluster of differentiation 81; TSG101: tumor susceptibility gene 101; HSP70: heat shock protein 70; BSA: bovine serum albumin; Lamin A/C: lamin A and lamin C; MFI: mean fluorescence intensity; IgG: immunoglobulin G; CD90: cluster of differentiation 90; β-actin: beta-actin; PE-A: phycoerythrin area; FLAG: FLAG epitope tag.

Comparisons between two groups were performed using Student's t-test. Comparisons involving three or more groups were analyzed using one-way or two-way analysis of variance (ANOVA), as appropriate to the experimental design, followed by multiple-comparison tests as specified in the corresponding figure legends. A P-value < 0.05 was considered statistically significant.

RESULTS

Generation of PSMA-scFv-engineered EV-producing cells

PSMA is highly elevated in advanced and CRPC, making it an attractive target for tumor-selective delivery[15]. To establish a PSMA-targeted EV platform, we engineered EV-producing cells to express a PSMA-targeting scFv (PSMA-scFv) fused to LAMP2B, enabling surface display of PSMA-scFv on secreted vesicles[16] [Figure 1A]. The expression of the resulting PSMA-scFv-LAMP2B construct was initially validated in HEK293A cells. Western blot analysis demonstrated robust expression of LAMP2B in both whole-cell lysates and corresponding EV fractions of PSMA-scFv-LAMP2B- and LAMP2B-engineered samples. A distinct band at the expected molecular weight of the fusion protein (~150 kDa) was detected in PSMA-scFv-LAMP2B-transfected samples but not in parental and LAMP2B controls, confirming successful incorporation of PSMA-scFv into EVs [Figure 1B]. MSCs are increasingly recognized for their intrinsic therapeutic properties, including immunomodulatory capacity and tumor-homing potential. We next established stable expression of PSMA-scFv-LAMP2B in MSCs, the intended EV-producing cell source. Consistent with the HEK293A validation, the PSMA-scFv-LAMP2B fusion protein was readily detected in both MSC lysates and EV [Figure 1C] fractions, indicating efficient expression and vesicular incorporation of the engineered construct.

Characterization of PSMA-scFv-engineered MSC-derived EVs

Having established stable expression and EV incorporation of PSMA-scFv, we next evaluated the structural and functional characteristics of the engineered EVs. To confirm EV identity and purity, we performed comprehensive protein characterization of EVs that were derived from parental, LAMP2B-expressing (LAMP2B), and PSMA-scFv-LAMP2B-expressing MSCs in accordance with the Minimal Information for Studies of Extracellular Vesicles (MISEV) 2023 guidelines[17]. EV marker analysis confirmed the presence of canonical EV proteins, including CD63, CD9, CD81, TSG101, β-actin and HSP70, and the absence of cellular contaminants, such as the endoplasmic reticulum marker calnexin and nuclear marker lamin A/C, consistent with MISEV 2023 guidelines. In addition, the MSC marker CD90 was detected, supporting the cellular origin of EVs, while BSA was not detected in EV fractions, indicating minimal contamination from culture media [Figure 1C]. NTA demonstrated that MSC-derived EVs, including EV-Parental, EV-LAMP2B, and EV-PSMA^{scFv}, exhibited comparable size distributions, predominantly within the 50-400 nm range, with a peak around ~100 nm [Figure 1D]. TEM further confirmed the characteristic spherical morphology and bilayer membrane structure of EVs across all groups, indicating that genetic modification did not alter vesicle integrity [Figure 1E]. To determine whether PSMA-scFv was correctly displayed on the EV surface, we performed Protein L binding assays [Supplementary Figure 1A]. Flow cytometric analysis revealed a marked increase in PE-labeled Protein L binding in EV-PSMA^{scFv} compared with EV-parental and EV-LAMP2B

controls, as evidenced by a rightward shift in fluorescence intensity and a significantly higher proportion of Protein L-positive events [Figure 1F]. Quantitative flow cytometry [Supplementary Figure 1B] and optical density (OD) [Supplementary Figure 1C] analyses further demonstrated significantly greater PE-Protein L binding in EV-PSMA^{scFv} than in EV-parental and EV-LAMP2B controls. Given that Protein L specifically binds to the κ light chain of antibody fragments, these findings confirm successful surface localization and proper extracellular orientation of the PSMA-scFv on engineered EVs and siRNA encapsulated EVs. Collectively, these results demonstrate that PSMA-scFv engineering and cargo loading do not alter EV structural integrity while enabling functional surface display of the targeting ligand.

PSMA expression determines selective binding of EV-PSMA^{scFv} to prostate cancer cells

To evaluate targeting specificity across clinically relevant prostate cancer subtypes, we selected cell line models representing distinct stages of disease progression. LNCaP, which is an androgen receptor (AR)-positive and androgen-sensitive cell line originally derived from lymph node metastases of prostate cancer patients[18], was used as a model of high-risk HSPC. CWR22Rv1 cells, which retain AR signaling but exhibit androgen-independent growth due to constitutively active AR variants[19], were used to represent AR-positive CRPC. In contrast, PC3 and DU145 cells, which lack functional AR signaling and are androgen-independent, were used as models of AR-negative CRPC.

Flow cytometric analysis first confirmed differential PSMA surface expression among these prostate cancer models. LNCaP cells exhibited high PSMA expression, whereas CWR22Rv1 cells showed moderate expression. In contrast, PSMA expression was undetectable in PC3 and DU145 cells [Figure 2A and B]. We next evaluated whether PSMA-scFv functionalization enhanced EV binding in a PSMA-dependent manner. Baseline signal intensity of labeled EVs was confirmed to be comparable across preparations prior to cell exposure, as indicated by similar absorbance values [Supplementary Figure 2A]. Following incubation with EV-PSMA^{scFv}, PSMA-expressing LNCaP and CWR22Rv1 cells exhibited significantly increased EV binding compared with EV-Parental and EV-LAMP2B controls [Supplementary Figure 2B]. In contrast, PSMA-negative PC3 and DU145 cells showed no difference in EV binding among the three types of EVs. Consistently, flow cytometry analysis, which independently assessed EV binding at the single-cell level, demonstrated significantly higher populations of EV-positive cells and increased mean fluorescence intensity (MFI) in LNCaP and CWR22Rv1 cells following exposure to EV-PSMA^{scFv}, whereas no significant enhancement was observed in PC3 or DU145 cells [Figure 2C and D]. Notably, measurable basal EV binding was observed in the PSMA-negative PC3 and DU145 cells across all EV preparations, indicating that PSMA-scFv functionalization does not eliminate the intrinsic PSMA-independent interactions of MSC-derived EVs with tumor cells. The magnitude of this basal EV association varied among prostate cancer cell lines, suggesting cell context-dependent differences in intrinsic MSC-EV interactions. Nevertheless, PSMA-scFv functionalization provides an additional PSMA-dependent enhancement of EV binding, as supported by the relationship between EV binding and relative PSMA surface expression across the prostate cancer cell lines. To directly determine whether EV binding is dependent on PSMA expression, we next employed both loss- and gain-of-function approaches in prostate cancer cell models. Flow cytometric analysis confirmed efficient modulation of PSMA expression. In LNCaP cells, PSMA surface expression was markedly reduced following siRNA-mediated knockdown (siPSMA) compared with non-targeting control (siNC) and mock-transfected cells, as evidenced by decreased fluorescence intensity [Figure 3A]. Conversely, stable expression of PSMA in PC3 cells resulted in elevated PSMA surface expression relative to wild-type controls [Figure 3B]. We next assessed the binding of EV-PSMA^{scFv} to these PSMA-modified cells. In LNCaP cells, PSMA knockdown significantly impaired EV binding, as demonstrated by reduced EV positive populations and lower MFI compared with mock and siNC controls [Figure 3C and D]. In contrast, PSMA overexpression in PC3 cells significantly enhanced EV binding relative to wild-type cells [Figure 3E and F]. Collectively, these findings demonstrate that binding of PSMA^{scFv}-engineered EVs is directly dependent on surface PSMA expression, establishing PSMA as a functional determinant of EV targeting specificity.

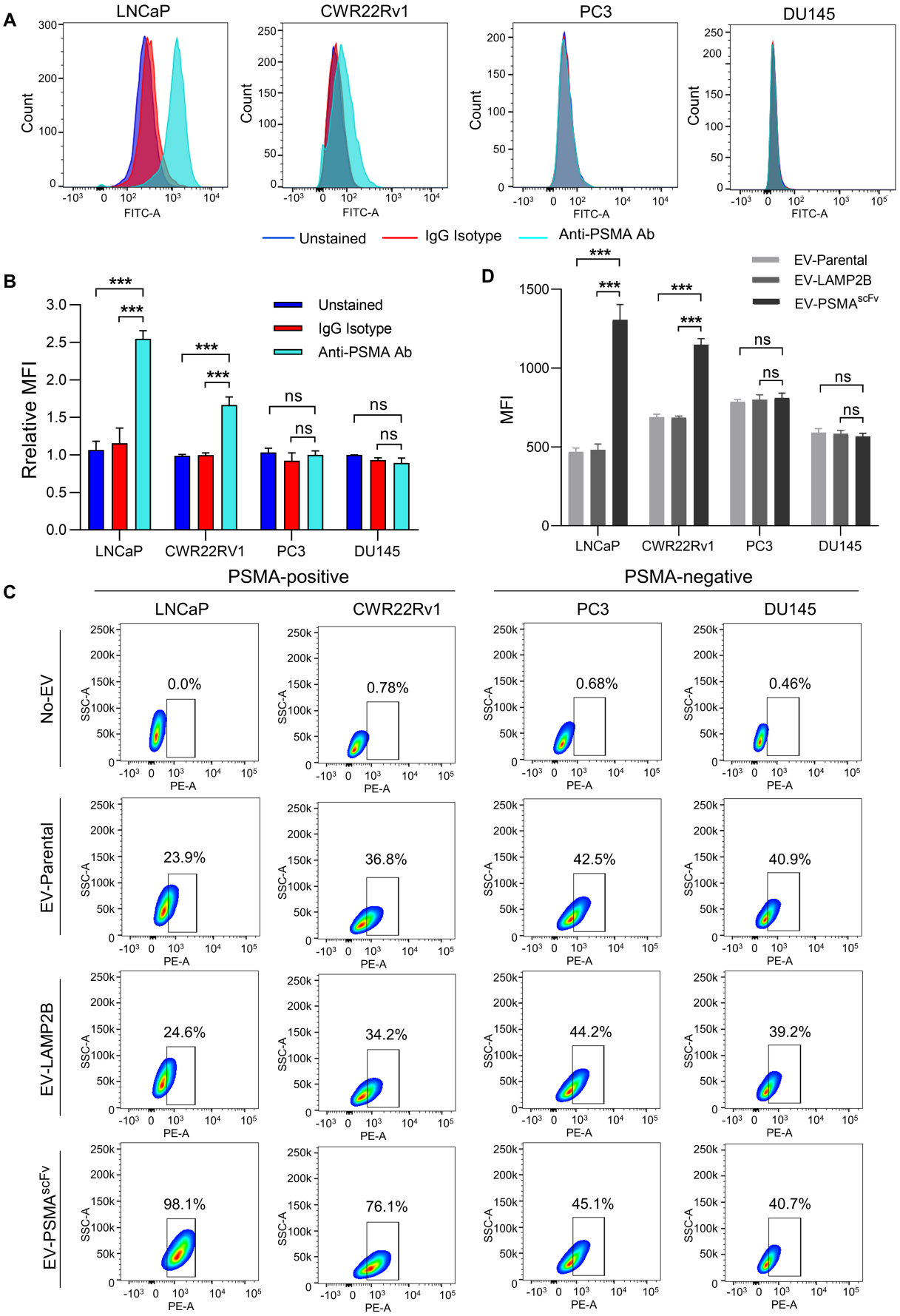


Figure 2. Selective binding of EV-PSMA^{scFv} to PSMA-expressing prostate cancer cells. (A) Flow cytometric analysis of surface PSMA expression in prostate cancer cell lines. Representative histograms of anti-PSMA antibody staining in LNCaP, CWR22Rv1, PC3, and DU145 cells. Unstained and IgG isotype controls are shown; (B) Quantification of relative MFI of PSMA expression in prostate cancer cell lines; (C

and D) Flow cytometric analysis of cell-associated EV binding at the single-cell level in prostate cancer cells following exposure to labeled EVs. Representative dot plots show gated EV-positive cell populations, with percentages indicating EV-bound cells among total analyzed cells (C). Quantification of EV-associated MFI is shown in (D). Representative flow cytometry plots are shown. Experiments were conducted in three independent biological repeats ($n = 3$), with each repeat using an independently prepared EV batch and analyzed in triplicate. Statistical analysis was performed using two-way ANOVA followed by Šídák's multiple-comparisons test for the indicated comparisons. ns, not significant; $^{***}P < 0.001$. EVs: Extracellular vesicles; PSMA: prostate-specific membrane antigen; MFI: mean fluorescence intensity; IgG: immunoglobulin G; PE: phycoerythrin; ANOVA: analysis of variance; EV-PSMA^{scFv}: extracellular vesicles displaying PSMA-targeting single-chain variable fragments; FITC-A: fluorescein isothiocyanate area; PE-A: phycoerythrin area.

PSMA-dependent uptake of EV-PSMA^{scFv} in prostate cancer cells

To determine whether PSMA-dependent binding translates into enhanced cellular uptake, we next evaluated the internalization of engineered EVs in prostate cancer cell models. Intracellular distribution of EVs was assessed by confocal microscopy following incubation with ExoSparkler-labeled EVs. In PSMA-positive LNCaP cells, EV-PSMA^{scFv} exhibited markedly increased intracellular accumulation with predominantly cytoplasmic localization compared with EV-parental and EV-LAMP2B controls [Figure 4A]. Quantitative analysis demonstrated an approximately two-fold increase in mean EV-associated fluorescence intensity per cell following exposure to EV-PSMA^{scFv} relative to control EV groups [Figure 4B]. In contrast, PSMA-negative PC3 cells exhibited minimal differences in EV internalization among these three EV preparations, with no significant change in EV-associated fluorescence intensity per cell [Figure 4C and D].

To further establish the role of PSMA in EV uptake, confocal microscopy was performed using complementary PSMA loss- and gain-of-function models. PSMA knockdown in LNCaP cells reduced EV-PSMA^{scFv}-associated intracellular fluorescence [Supplementary Figure 3A and B], whereas ectopic PSMA expression in PC3 cells enhanced intracellular EV-PSMA^{scFv} fluorescence compared with the corresponding controls [Supplementary Figure 4A and B]. Confocal z-stack imaging and orthogonal reconstruction further demonstrated EV-associated fluorescence within the cell, supporting intracellular localization of EV-PSMA^{scFv} [Supplementary Figure 5]. These findings demonstrate that PSMA^{scFv} engineering enhances EV uptake in a PSMA-dependent manner, linking receptor-specific binding to efficient intracellular delivery in prostate cancer cells.

Encapsulation, protection, and functional delivery of siADAM9 by EV-PSMA^{scFv}

Having established PSMA-dependent binding and uptake of engineered EVs, we next evaluated their capacity to encapsulate and protect therapeutic siRNA cargo. EV-PSMA^{scFv} were loaded with siADAM9 (two independent sequences), and encapsulation efficiency was assessed by quantitative PCR analysis. Encapsulation efficiency was assessed by quantitative PCR analysis. The analysis demonstrated that approximately 250-300 siRNA copies per EV particle were encapsulated [Figure 5A], corresponding to an estimated 10% of the input siRNA being successfully encapsulated [Figure 5B]. Moreover, compared with naked siRNA, EV-encapsulated siADAM9 exhibited markedly enhanced resistance to RNase-mediated degradation, as evidenced by significantly lower Cq values following RNase exposure [Figure 5C]. These findings indicate that EV encapsulation effectively protects siRNA cargo from extracellular degradation. To determine whether siRNA loading affects the targeting specificity of EV-PSMA^{scFv}, we evaluated the binding of siADAM9-loaded EV-PSMA^{scFv} using the PSMA loss- and gain-of-function models described above. PSMA knockdown significantly reduced the binding of siADAM9-loaded EV-PSMA^{scFv} in LNCaP cells compared with mock and siNC controls [Supplementary Figure 6A and B]. Conversely, ectopic PSMA expression markedly enhanced EV binding in PC3 cells relative to wild-type (WT) cells [Supplementary Figure 6C and D], indicating that PSMA-dependent targeting is retained following siADAM9 loading. These results demonstrate that PSMA-dependent targeting is retained following siADAM9 loading, indicating that therapeutic cargo incorporation does not compromise the receptor-specific binding of EV-PSMA^{scFv}.

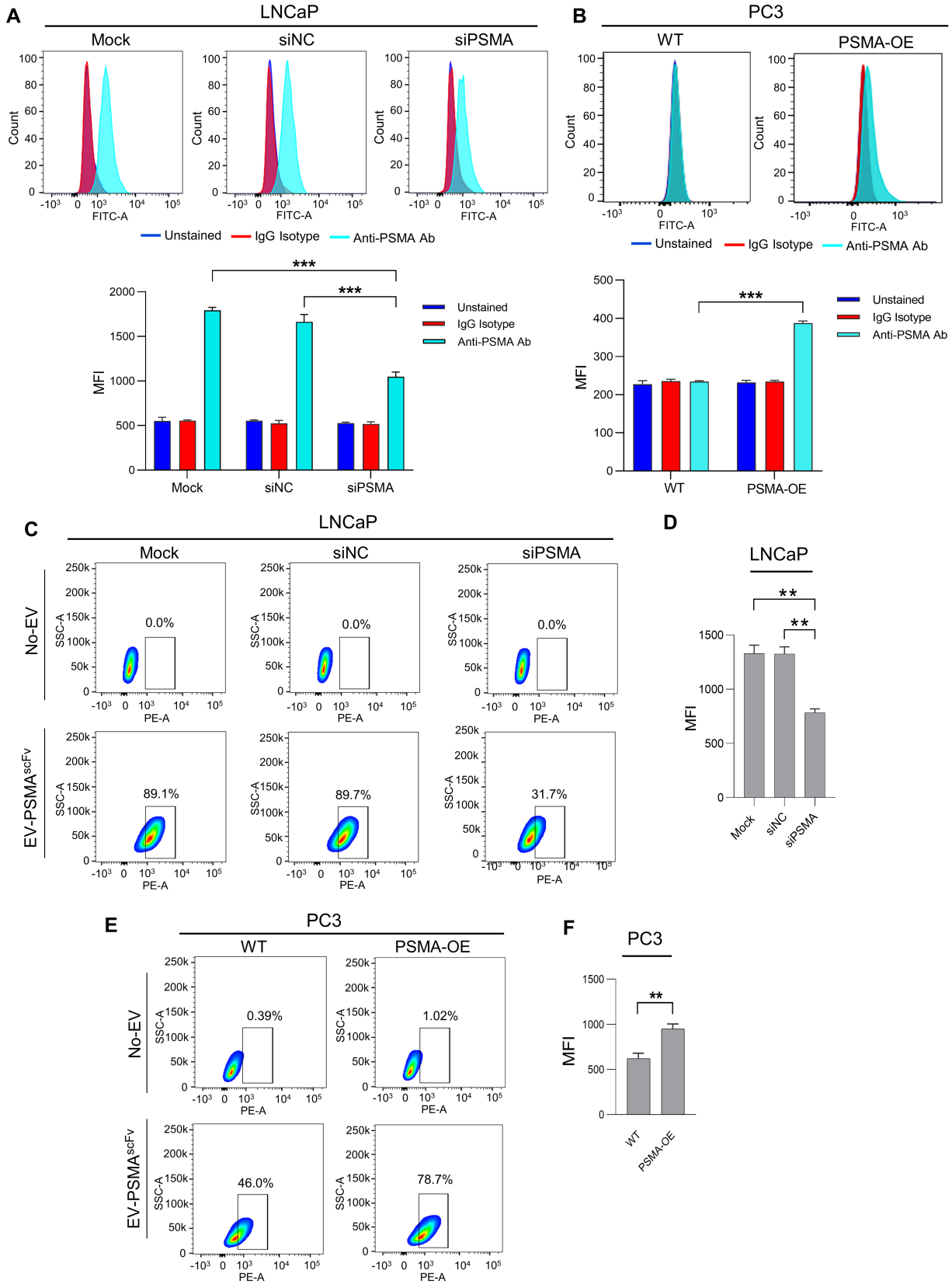


Figure 3. PSMA expression determines binding efficiency of EV-PSMA^{scFv}. (A) Flow cytometric analysis of surface PSMA expression in LNCaP cells following siRNA-mediated PSMA knockdown (siPSMA). Mock-transfected and siNC controls are shown. Representative histograms and quantification of MFI are presented; (B) Flow cytometric analysis of PSMA surface expression in WT and PSMA-OE PC3 cells. Representative histograms and quantification of MFI are shown; (C and D) Flow cytometric analysis of EV binding in mock-, siNC-, and siPSMA-treated LNCaP cells following exposure to labeled EV-PSMA^{scFv}. Representative dot plots (C) and quantitative analysis of MFI (D) are shown; (E and F) Flow cytometric analysis of EV binding in WT and PSMA-OE PC3 cells following exposure to labeled EV-PSMA^{scFv}. Representative dot plots (E) and quantitative analysis of MFI (F) are shown. Data were obtained from three independent biological repeats (n = 3), with each repeat using a separately prepared EV batch and analyzed in triplicate. Statistical analysis was

performed using two-way ANOVA followed by Šídák's multiple-comparisons test (A and B), one-way ANOVA followed by Tukey's multiple-comparisons test (D), and Student's *t*-test (F). ns, not significant; $^{**}P < 0.01$; $^{***}P < 0.001$. EVs: Extracellular vesicles; PSMA: prostate-specific membrane antigen; siRNA: small interfering RNA; siPSMA: PSMA-targeting small interfering RNA; siNC: non-targeting small interfering RNA control; WT: wild-type; PSMA-OE: PSMA-overexpressing; MFI: mean fluorescence intensity; ANOVA: analysis of variance; EV-PSMA^{scFv}: extracellular vesicles displaying PSMA-targeting single-chain variable fragments; FITC-A: fluorescein isothiocyanate area; PE-A: phycoerythrin area.

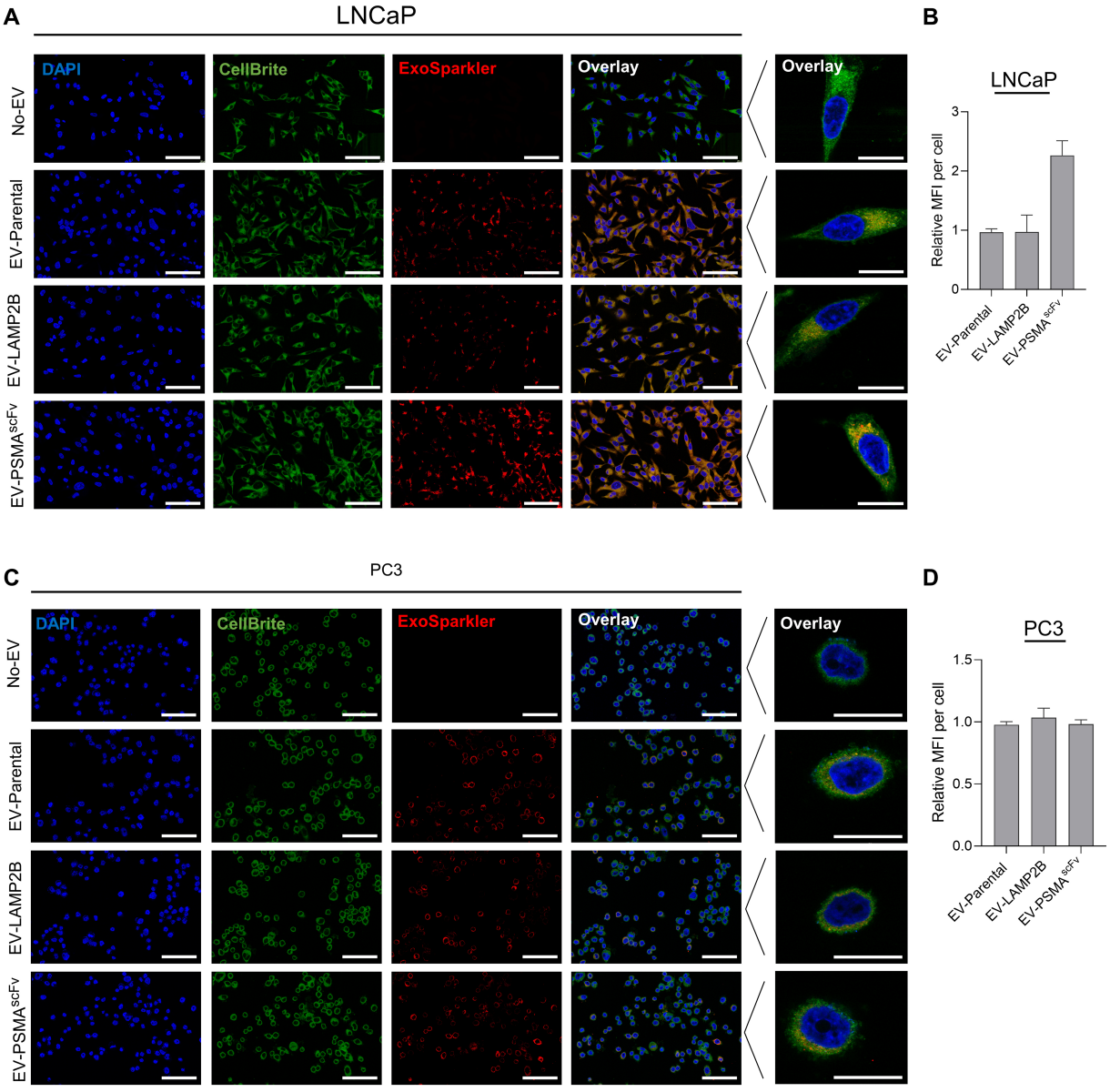


Figure 4. Intracellular uptake of EV-PSMA^{scFv} in prostate cancer cells. (A and C) Confocal microscopy analysis of EV uptake in PSMA-positive LNCaP (A) and PSMA-negative PC3 (C) cells following incubation with ExoSparkler-labeled Parental, LAMP2B, or PSMA^{scFv} EVs. Nuclei were stained with DAPI (blue), cell membranes with CellBrite™ Green (green), and EVs are shown in red. Representative merged images and high-magnification single-cell images are shown. Scale bars: 100 μm (merged images) and 20 μm (high-magnification images); (B and D) Quantitative analysis of EV-associated fluorescence intensity per cell in LNCaP (B) and PC3 (D) cells following exposure to labeled EVs. Fluorescence intensity was quantified from three fields of view acquired from a single experimental sample using one EV preparation. The three fields of view represent technical measurements rather than independent biological replicates. Data are presented as mean ± SD of the three technical measurements. Representative confocal microscopy images are shown. EVs: Extracellular vesicles; PSMA: prostate-specific membrane antigen; scFv: single-chain variable fragment; LAMP2B: lysosome-associated membrane protein 2B; DAPI: 4′,6-diamidino-2-phenylindole; SD: standard deviation; MFI: mean fluorescence intensity; EV-PSMA^{scFv}: extracellular vesicles displaying PSMA-targeting single-chain variable fragments.

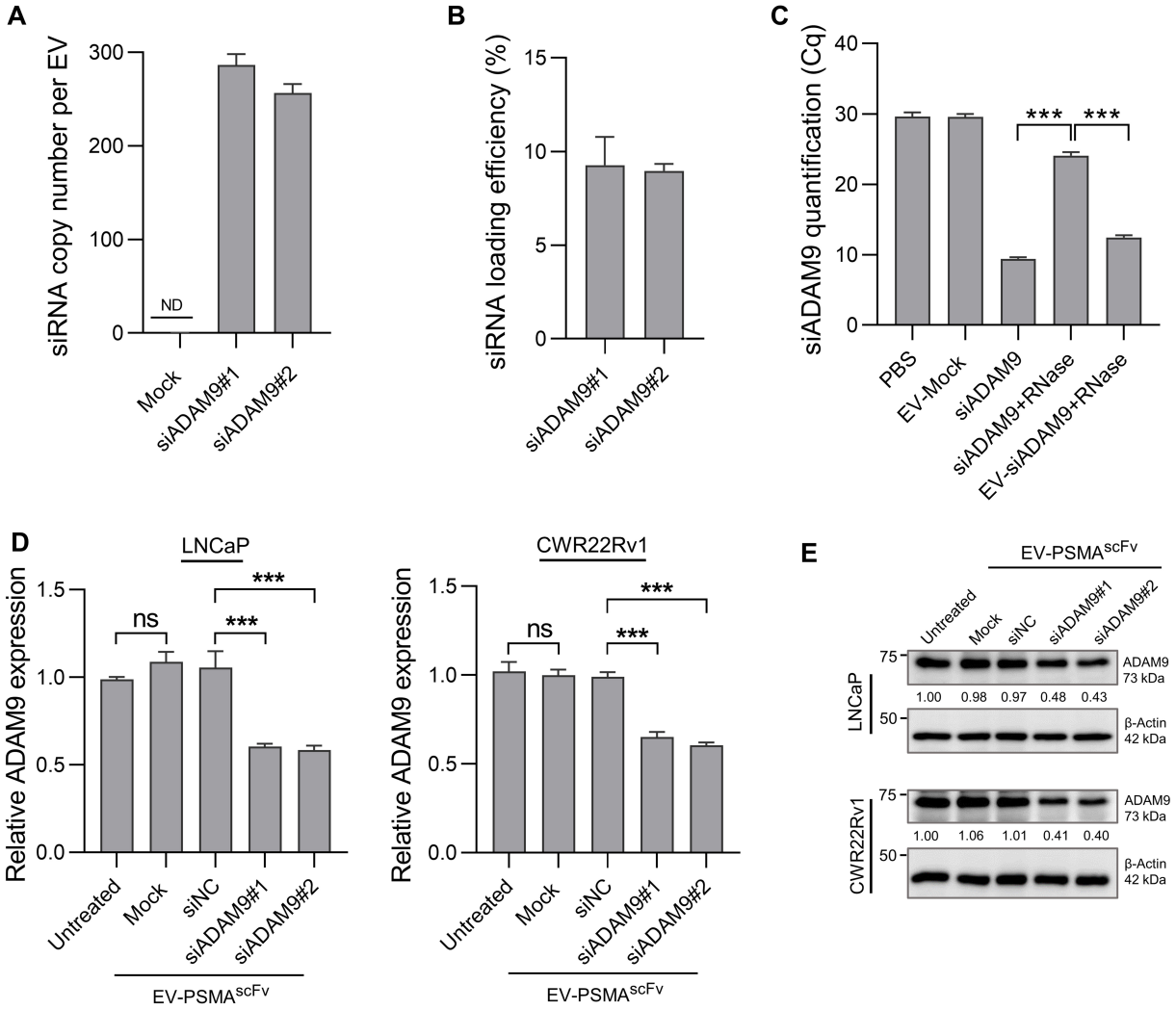


Figure 5. Characterization of siADAM9 encapsulation, stability, and target gene silencing mediated by EV-PSMA^{scFv}. (A) Quantification of siRNA copy number per EV particle following encapsulation of siADAM9 variants (#1 and #2). ND; (B) Encapsulation efficiency of siADAM9 in EV-PSMA^{scFv} determined by qPCR analysis, relative to input naked siRNA; (C) RNase protection assay. Naked or EV-encapsulated siADAM9 was exposed to exogenous RNase prior to qPCR analysis. EV encapsulation protected siADAM9 from RNase-mediated degradation, as indicated by lower Cq values compared with naked siRNA controls; (D) RT-qPCR analysis of ADAM9 mRNA expression in LNCaP and CWR22Rv1 cells following treatment with EV-PSMA^{scFv} loaded with siADAM9 or siNC. Unloaded EVs and mock-treated cells served as controls; (E) Immunoblot analysis of ADAM9 protein expression in LNCaP and CWR22Rv1 cells following treatment with siADAM9-loaded EV-PSMA^{scFv}. β-Actin served as the loading control. Relative protein expression levels normalized to β-actin are indicated below the blots. Experiments were conducted in three independent biological repeats (n = 3), each using an independently prepared EV batch, with analyses performed in triplicate where applicable. Data are presented as mean ± SD. Statistical analysis was performed using one-way ANOVA followed by Šídák's multiple-comparisons test for the indicated comparisons. ns, not significant; $^{***}P < 0.001$. EVs: Extracellular vesicles; PSMA: prostate-specific membrane antigen; siRNA: small interfering RNA; siADAM9: ADAM9-targeting small interfering RNA; siNC: non-targeting small interfering RNA control; ND: not detected; RNase: ribonuclease; qPCR: quantitative polymerase chain reaction; Cq: quantification cycle; RT-qPCR: reverse transcription quantitative polymerase chain reaction; SD: standard deviation; ANOVA: analysis of variance; β-actin: beta-actin; EV-PSMA^{scFv}: extracellular vesicles displaying PSMA-targeting single-chain variable fragments.

To further assess the reproducibility of the engineered EV platform, an independently prepared batch of siADAM9-loaded EV-PSMA^{scFv} was characterized. The immunoblotting confirmed incorporation of the PSMA-scFv-LAMP2B fusion protein [Supplementary Figure 7A]. The EV proteomic characterization was also carried out in the siADAM9 encapsulated samples [Supplementary Figure 7B]. NTA demonstrated comparable particle size characteristics [Supplementary Figure 7C and D], while Protein L binding analysis further demonstrated surface-accessible scFv display, consistent with that observed in the original EV

preparation [Supplementary Figure 8A-D]. Together, these findings support the reproducibility of PSMA-scFv incorporation and surface display across independent EV preparations.

We next evaluated whether EV-PSMA^{scFv}-mediated delivery of siADAM9 resulted in functional gene silencing in recipient prostate cancer cells. Treatment with EV-PSMA^{scFv} loaded with siADAM9 significantly reduced ADAM9 messenger RNA (mRNA) expression in both LNCaP and CWR22Rv1 cells compared with unloaded EVs, mock-treated cells, and EVs loaded with non-targeting siRNA (siNC) [Figure 5D]. Consistently, immunoblot analysis confirmed substantial suppression of ADAM9 protein expression following treatment with siADAM9-loaded EV-PSMA^{scFv} in both prostate cancer models [Figure 5E]. Notably, the two independent ADAM9-targeting siRNAs, siADAM9#1 and siADAM9#2 (sequences provided in Supplementary Table 1), exhibited comparable silencing activity, reducing ADAM9 protein expression to similar levels in both LNCaP and CWR22Rv1 cells. EV-PSMA^{scFv} efficiently encapsulates and protects siRNA cargo while enabling functional intracellular delivery and robust target gene silencing in prostate cancer cells.

Targeted delivery of siADAM9 via EV-PSMA^{scFv} suppresses aggressive phenotypes and stemness-associated programs in prostate cancer cells

To determine whether EV-PSMA^{scFv}-mediated delivery of siADAM9 affects cell migratory behavior, LNCaP and CWR22Rv1 cells were treated with EV-PSMA^{scFv} loaded with siADAM9, siNC, or unloaded EVs. Wound healing assays demonstrated that EV-mediated ADAM9 silencing significantly reduced wound closure in both prostate cancer cell lines within 24-48 h, indicating impaired migratory capacity following siADAM9 delivery [Figure 6A and B]. Consistent with these findings, Transwell assays revealed a significant reduction in the number of migrated cells following siADAM9-loaded EV-PSMA^{scFv} treatment compared with control groups [Figure 6C and D]. In contrast, siNC-loaded and unloaded EVs showed minimal effects on cell migration. To further investigate whether the reduced migratory phenotype was associated with epithelial-mesenchymal transition (EMT) remodeling, we next examined the expression of key EMT- and extracellular matrix-associated markers following treatment with siADAM9-loaded EV-PSMA^{scFv}. In both LNCaP and CWR22Rv1 cells, EV-PSMA^{scFv}-mediated siADAM9 silencing increased expression of the epithelial marker E-cadherin while reducing expression of the mesenchymal markers such as vimentin and N-cadherin. In parallel, expression of the matrix remodeling proteins MMP2 and MMP9 was decreased, whereas the matrix metalloproteinase inhibitor TIMP3 was increased following siADAM9 delivery, indicating suppression of extracellular matrix remodeling programs associated with tumor progression and migratory potential [Figure 6E and F].

Given the critical role of stemness-associated programs in prostate cancer progression, including their contributions to cellular plasticity, metastatic potential, and therapeutic resistance, we next investigated the effects of EV-mediated ADAM9 silencing on these aggressive tumor phenotypes. Cell proliferation assays first demonstrated that treatment with siADAM9-loaded EV-PSMA^{scFv} significantly reduced cell growth in both LNCaP and CWR22Rv1 cells under monolayer culture conditions compared with control treatments [Supplementary Figure 9]. Notably, significant suppression of cell proliferation became evident at later time points, suggesting that the early reduction in wound closure was unlikely to be attributable solely to reduced proliferation. To further evaluate tumor stemness-associated properties, sphere formation assays were performed under three-dimensional culture conditions. Treatment with siADAM9-loaded EV-PSMA^{scFv} significantly reduced both the number and size of tumor spheres in LNCaP and CWR22Rv1 cells, indicating impaired sphere-forming and tumor-propagating capacity following ADAM9 silencing [Figure 7A and B]. Consistent with these phenotypic changes, expression of key stemness-associated regulators, including SOX2, OCT4 and BMI1, was markedly reduced at both the mRNA and protein levels in response to siADAM9 delivery compared with control groups [Figure 7C-F]. Notably, efficient suppression of ADAM9

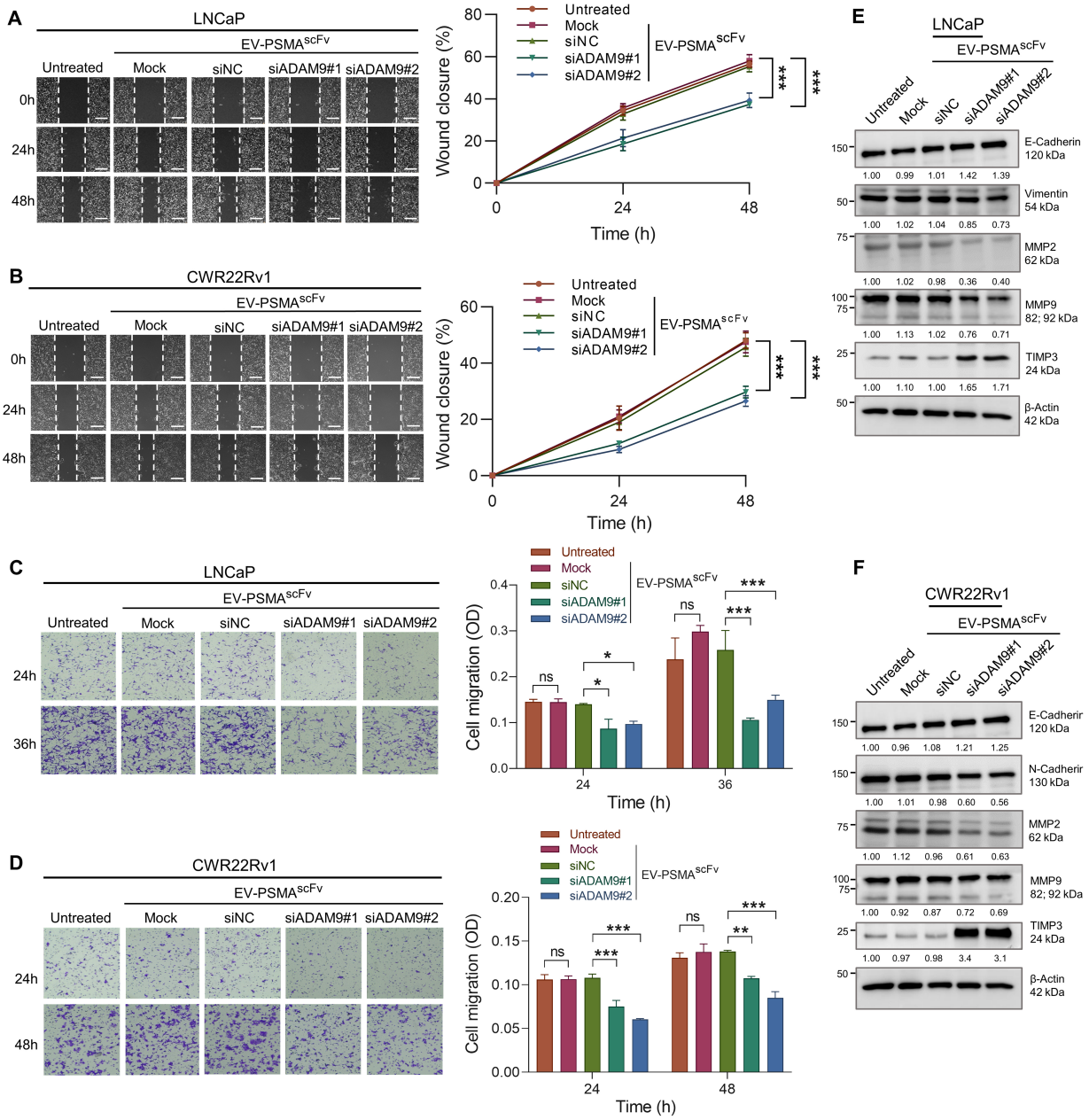


Figure 6. EV-PSMA^{scFv}-mediated ADAM9 silencing effects on migration and EMT-associated remodeling in prostate cancer cells. (A and B) Wound healing assays in LNCaP (A) and CWR22Rv1 (B) cells following treatment with EV-PSMA^{scFv} loaded with siADAM9 variants (#1 and #2), non-targeting siRNA (siNC), or unloaded EVs. Representative images were captured at the indicated time points, and wound closure percentages were quantified. Dashed lines indicate wound boundaries (scale bars: 500 μm); (C and D) Transwell migration assays in LNCaP (C) and CWR22Rv1 (D) cells following treatment with siADAM9-loaded EV-PSMA^{scFv} or control EV preparations. Representative images of migrated cells are shown alongside quantitative analysis of cell migration based on the absorbance of solubilized crystal violet; (E and F) Immunoblot analysis of EMT- and ECM-associated proteins in LNCaP (E) and CWR22Rv1 (F) cells following treatment with siADAM9-loaded EV-PSMA^{scFv}. Expression levels of E-cadherin, N-cadherin, MMP2, MMP9, TIMP3, and β-actin were evaluated. Relative protein expression levels normalized to β-actin are indicated below the blots. Representative images are shown. Data were obtained from three independent biological repeats, each using a separately prepared EV batch (n = 3 biological replicates; 3 independent EV preparations), with measurements performed in triplicate. Statistical analysis was performed using two-way ANOVA followed by Šídák's multiple-comparisons test. ns, not significant; $^{**}P < 0.01$; $^{***}P < 0.001$. EVs: Extracellular vesicles; PSMA: prostate-specific membrane antigen; siADAM9: ADAM9-targeting small interfering RNA; siNC: non-targeting small interfering RNA control; EMT: epithelial-mesenchymal transition; ECM: extracellular matrix; MMP2: matrix metalloproteinase 2; MMP9: matrix metalloproteinase 9; TIMP3: TIMP metallopeptidase inhibitor 3; SD: standard deviation; ANOVA: analysis of variance; β-actin: beta-actin; EV-PSMA^{scFv}: extracellular vesicles displaying PSMA-targeting single-chain variable fragments.

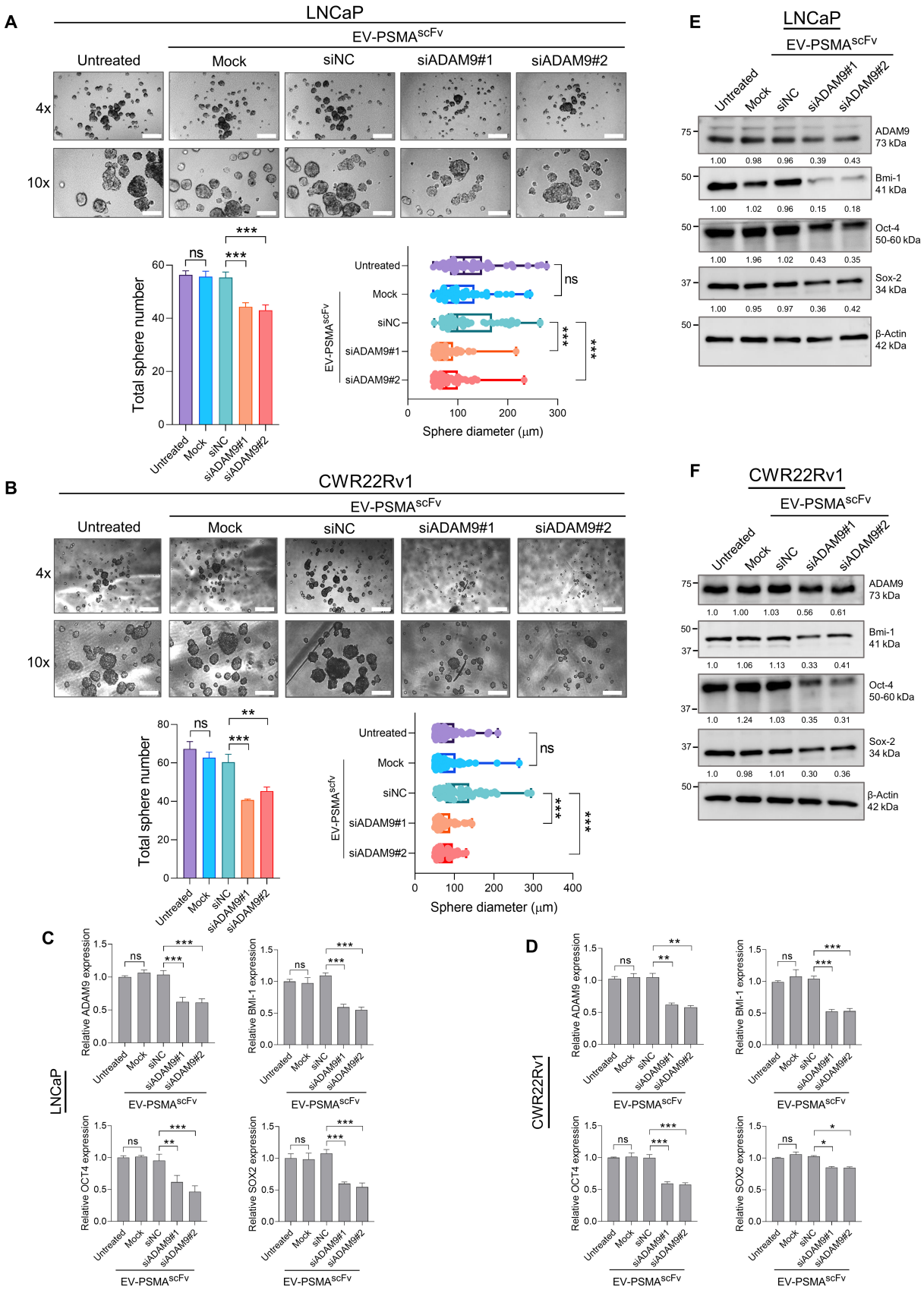


Figure 7. Effects of EV-PSMA^{scFv}-mediated ADAM9 silencing on sphere formation stemness-associated programs in prostate cancer. (A and B) Sphere formation assays in LNCaP (A) and CWR22Rv1 (B) cells following treatment with EV-PSMA^{scFv} loaded with siADAM9 variants (#1 and #2), non-targeting siRNA (siNC), or unloaded EVs. Representative images of tumor spheres are shown alongside quantitative analysis of sphere number and sphere size distribution. Scale bars: 500 μm; (C and D) RT-qPCR analysis of stemness-associated gene expression in LNCaP (C) and CWR22Rv1 (D) sphere cultures following treatment with siADAM9-loaded EV-PSMA^{scFv}. Expression levels of SOX2, OCT4, NANOG, BMI1, and ADAM9 were evaluated; (E and F) Immunoblot analysis of stemness-associated

proteins in LNCaP (E) and CWR22Rv1 (F) sphere cultures following treatment with siADAM9-loaded EV-PSMA^{scFv}. Expression levels of SOX2, OCT4, NANOG, BMI1, ADAM9, and β-actin were analyzed. Relative protein expression levels normalized to β-actin are indicated below the blots. Results were obtained from three independent biological experiments (n = 3), each using an independently prepared EV batch, with analyses performed in triplicate. Statistical analysis was performed using one-way ANOVA followed by Šídák's multiple-comparisons test for the indicated comparisons. ns, not significant; $^{*}P < 0.05$; $^{***}P < 0.001$. EVs: Extracellular vesicles; PSMA: prostate-specific membrane antigen; siADAM9: ADAM9-targeting small interfering RNA; siNC: non-targeting small interfering RNA control; RT-qPCR: reverse transcription quantitative polymerase chain reaction; SOX2: SRY-box transcription factor 2; OCT4: octamer-binding transcription factor 4; NANOG: Nanog homeobox; BMI1: BMI1 proto-oncogene, polycomb ring finger; ADAM9: a disintegrin and metalloproteinase 9; SD: standard deviation; ANOVA: analysis of variance; β-actin: beta-actin; EV-PSMA^{scFv}: extracellular vesicles displaying PSMA-targeting single-chain variable fragments.

expression was maintained under sphere culture conditions, indicating that EV-PSMA^{scFv}-mediated siRNA delivery remains effective within structurally complex three-dimensional tumor-like environments. Collectively, these findings demonstrate that EV-PSMA^{scFv}-mediated ADAM9 silencing suppresses aggressive tumor phenotypes, including migration and tumor propagation, while reversing EMT- and stemness-associated molecular programs in both hormone-sensitive and CRPC cells.

EV-PSMA^{scFv}-mediated ADAM9 silencing enhances androgen-targeted therapy through context-dependent suppression of adaptive resistance pathways

In current clinical practice, metastatic HSPC (HSPC) is commonly treated with ADT (ADT) in combination with androgen receptor pathway inhibitors; however, therapeutic resistance frequently develops. Based on our previous findings demonstrating that the ADAM9/UBN2/AKR1C3 axis contributes to the transition of androgen-dependent prostate cancer cells toward an androgen-independent state[7], we next investigated whether EV-mediated ADAM9 silencing could enhance responsiveness to androgen-targeted therapy in LNCaP cells. Cell viability assays demonstrated that treatment with siADAM9-loaded EV-PSMA^{scFv} further reduced cell survival compared with ADT monotherapy or combined ADT and abiraterone treatment alone [Figure 8A]. Correspondingly, although ADT alone or in combination with abiraterone induced marked upregulation of AKR1C3 relative to pre-treatment levels, EV-PSMA^{scFv}-mediated ADAM9 silencing significantly suppressed expression of ADAM9, UBN2, and AKR1C3 compared with siNC-loaded controls under androgen-targeted treatment conditions [Figure 8B and C]. In addition, the increased full-length androgen receptor (AR-FL) protein expression observed following androgen-targeted therapy was attenuated by siADAM9-loaded EV-PSMA^{scFv}, whereas androgen receptor splice variant 7 (AR-V7) remained undetectable under all conditions [Figure 8C].

To further evaluate therapeutic relevance in CRPC, where AR pathway inhibitors are commonly used as first-line systemic therapy, we next examined the effects of EV-PSMA^{scFv}-mediated ADAM9 silencing in CWR22Rv1 cells treated with abiraterone alone or combined ADT and abiraterone. Similar to the LNCaP model, addition of siADAM9-loaded EV-PSMA^{scFv} significantly reduced cell survival under androgen-targeted treatment conditions [Figure 8D]. Both siADAM9#1 and siADAM9#2 produced comparable enhancement of the treatment response, with no consistent difference in therapeutic effects between the two siRNAs. However, in contrast to the HSPC model, EV-mediated ADAM9 silencing in CWR22Rv1 cells exerted minimal effects on UBN2 and AKR1C3 expression despite partial induction of AKR1C3 following androgen-targeted therapy [Figure 8E and F]. Furthermore, AR-FL and AR-V7 protein levels remained elevated across all treatment conditions [Figure 8F], suggesting that ADAM9-mediated regulation of the UBN2/AKR1C3 axis preferentially operates within an androgen-responsive cellular context and is not maintained in androgen-independent CRPC cells. Notably, siADAM9 treatment was associated with increased p21 expression in both LNCaP and CWR22Rv1 cells, suggesting that modulation of cell cycle-associated pathways may represent a broader response to ADAM9 suppression rather than a mechanism specific to androgen-independent prostate cancer [Figure 8C and F]. These findings suggest that EV-PSMA^{scFv}-mediated ADAM9 silencing may enhance therapeutic responsiveness through distinct context-dependent mechanisms in HSPC and CRPC.

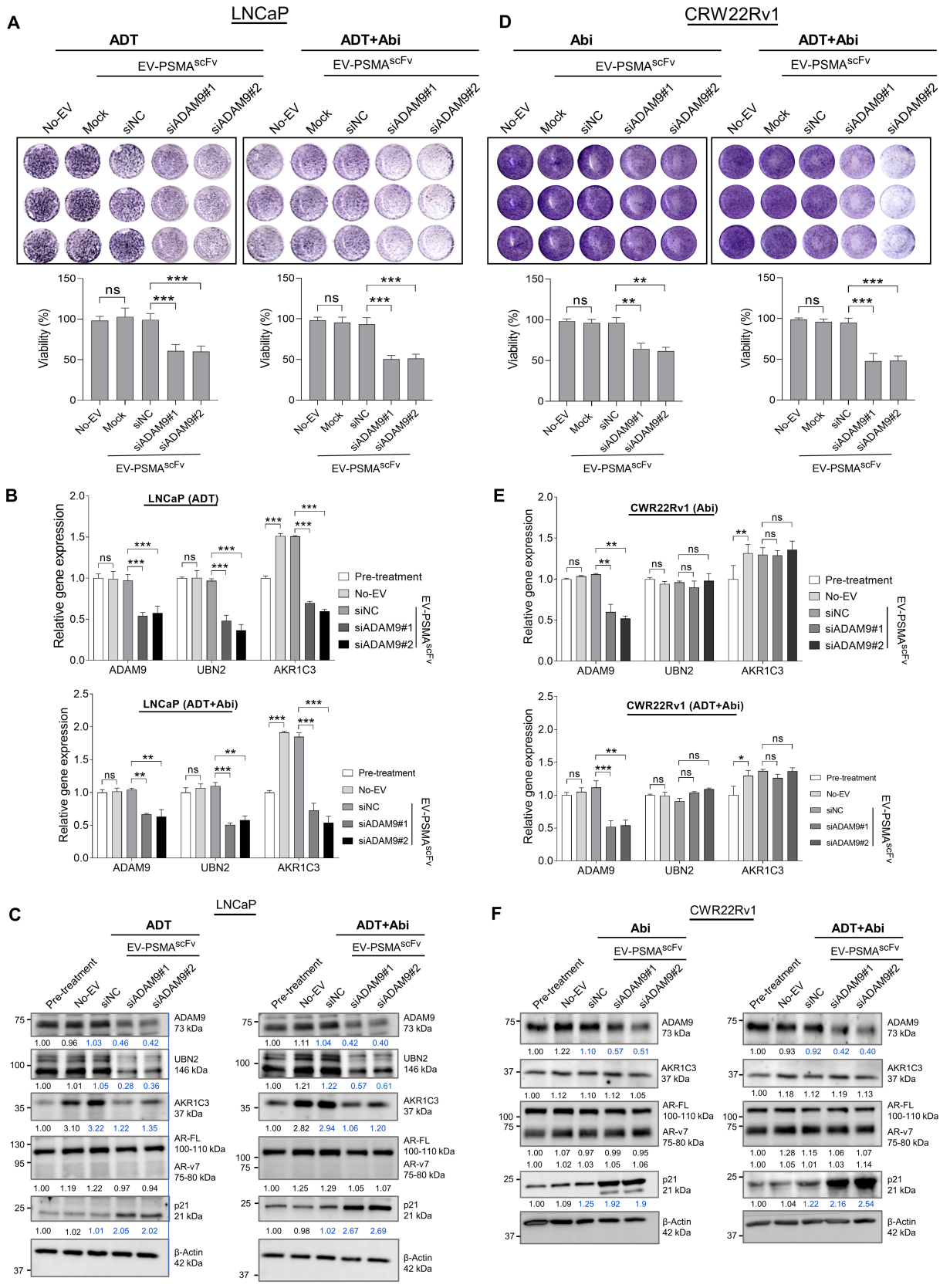


Figure 8. EV-PSMA^{scFv} ADAM9 silencing effects on androgen response and AR signaling in prostate cells. (A and D) Crystal violet viability assays in LNCaP (A) and CWR22Rv1 (D) cells following treatment with androgen-targeted therapies in combination with EV-PSMA^{scFv} loaded with siADAM9 variants (#1 and #2), non-targeting siRNA (siNC), or unloaded EVs. LNCaP cells were treated with ADT alone or combined ADT and Abi, whereas CWR22Rv1 cells were treated with abiraterone alone or combined ADT and abiraterone. Representative images and quantitative analysis of relative cell viability are shown; (B and E) RT-qPCR analysis of ADAM9, UBN2, and AKR1C3 expression in LNCaP (B) and CWR22Rv1 (E) cells following androgen-targeted treatment in combination with siADAM9-loaded EV-PSMA^{scFv} or control EV preparations. Relative gene expression was normalized to pre-treatment controls; (C and F) Immunoblot analysis of ADAM9-,

AR signaling-, and cell cycle-associated proteins in LNCaP (C) and CWR22Rv1 (F) cells following treatment with androgen-targeted therapies and siADAM9-loaded EV-PSMA^{scFv}. Expression levels of ADAM9, UBN2, AKR1C3, AR-FL, AR-V7, p21, and β-actin were analyzed. Relative protein expression levels normalized to β-actin and referenced to the pre-treatment group are indicated below the blots. AR-V7 was undetectable in LNCaP cells and therefore was not quantified. Both AR-FL and AR-V7 were quantified in CWR22Rv1 cells. Blue values highlight notable expression changes observed in siADAM9-loaded EV-treated groups compared with siNC controls. Data were generated from three independent biological replicates (n = 3), each using a separately prepared EV batch, with triplicate analyses where applicable. Statistical analysis was performed using one-way (A and D) and two-way (B and E) ANOVA followed by Šídák's multiple-comparisons test for the indicated comparisons. ns, not significant; $^{*}P < 0.05$; $^{**}P < 0.01$; $^{***}P < 0.001$. EVs: Extracellular vesicles; PSMA: prostate-specific membrane antigen; siADAM9: ADAM9-targeting small interfering RNA; siNC: non-targeting small interfering RNA control; ADT: androgen deprivation therapy; Abi: abiraterone; RT-qPCR: reverse transcription quantitative polymerase chain reaction; UBN2: ubinuclein 2; AKR1C3: aldo-keto reductase family 1 member C3; AR: androgen receptor; AR-FL: full-length androgen receptor; AR-V7: androgen receptor splice variant 7; p21: cyclin-dependent kinase inhibitor 1A; SD: standard deviation; ANOVA: analysis of variance; β-actin: beta-actin; EV-PSMA^{scFv}: extracellular vesicles displaying PSMA-targeting single-chain variable fragments.

DISCUSSION

Despite significant advances in ADT and next-generation AR-targeted agents, prostate cancer inevitably progresses to a treatment-resistant state. This transition is driven by adaptive molecular programs that restore AR signaling and promote tumor cell proliferation/survival[20]. RNA interference offers a highly specific strategy to suppress these adaptive resistance networks. However, its clinical translation is limited by poor systemic stability, rapid degradation, inefficient intracellular uptake, and lack of tumor specificity[21]. To overcome these barriers, there is a need for delivery systems capable of protecting RNA cargo while enabling efficient and selective intracellular delivery. In the present study, we developed a PSMA-targeted MSC-EV platform for delivery of siRNA against ADAM9 and demonstrated selective targeting, efficient intracellular delivery, and suppression of tumor-promoting pathways across both HSPC and CRPC models. Importantly, our findings demonstrate that receptor-directed EV engineering can enable selective and functional delivery of therapeutic siRNA, establishing the application of EV-mediated RNA interference in precision cancer therapy.

EVs represent a biologically derived delivery system, enabling protected and functional intracellular RNA delivery. A major limitation of EV-based therapeutics is the lack of target specificity, as native EVs are internalized by multiple cell types through diverse endocytic pathways, including clathrin- and caveolin-mediated endocytosis, phagocytosis, and macropinocytosis[22]. This non-selective uptake can reduce therapeutic efficiency and increase the risk of off-target effects. To enhance tumor-selective delivery, we fused PSMA-scFv to LAMP2B, enabling surface display of the targeting ligand while preserving EV integrity and ensuring its extracellular orientation. Our data demonstrate that engineering EVs with a PSMA-targeting scFv enabled selective binding and uptake in a PSMA expression-dependent manner, as confirmed by both gain- and loss-of-function approaches [Figure 3]. Given that PSMA undergoes efficient ligand-induced internalization, likely via clathrin-dependent endocytosis[23], PSMA-scFv functionalization can overcome the EV intrinsic limitation of non-specific uptake, thereby enhancing targeting precision and therapeutic efficiency.

Consistent with the enhanced targeting and cellular uptake achieved through PSMA-scFv functionalization, MSC-EV-mediated delivery of siADAM9 resulted in significant suppression of multiple tumorigenic phenotypes, including proliferation, migration, and stemness. Importantly, these effects were observed in both two-dimensional and three-dimensional culture systems [Figures 6 and 7], indicating that targeted EV delivery remains effective even within structurally complex tumor-like environments. The efficacy observed in spheroid models further suggests that engineered EVs may overcome physical barriers associated with tumor architecture, which often limit the penetration and distribution of conventional nanoparticle-based delivery systems. These findings indicate that targeted EVs support efficient intracellular delivery of biologically active siRNA capable of producing functional and sustained gene-silencing effects in clinically relevant tumor models.

In HSPC, early adaptive mechanisms, such as upregulation of key steroidogenic enzymes including AKR1C3, which enables continued intratumoral androgen production despite androgen deprivation[3], contribute to eventual treatment failure. Our findings demonstrate that combining PSMA-scFv-mediated ADAM9 silencing with ADT alone or ADT plus abiraterone results in enhanced suppression of tumor cell viability compared with standard therapy alone. EV-mediated ADAM9 silencing resulted in coordinated downregulation of UBN2 and AKR1C3 [Figure 8A-C], consistent with disruption of the ADAM9/UBN2/AKR1C3 axis characterized in our previous study[7]. In that study, AKR1C3 overexpression rescued the enhanced sensitivity of ADAM9- or UBN2-deficient LNCaP cells to androgen deprivation, supporting AKR1C3 as a functional downstream mediator of this pathway. While abiraterone inhibits CYP17A1-mediated androgen synthesis, ADAM9 silencing may complement this effect by attenuating the UBN2/AKR1C3 axis, which is implicated in compensatory intracrine androgen production. Thus, the present findings suggest that EV-mediated ADAM9 silencing may enhance the response to androgen-targeted therapy, at least in part, through modulation of this previously established resistance pathway. Notably, comparable downregulation of UBN2 and AKR1C3 was not observed in CWR22Rv1 cells, suggesting that the downstream consequences of ADAM9 silencing may differ according to prostate cancer cellular context. This difference may reflect the distinct AR and steroidogenic signaling states of the two models. Whereas LNCaP cells retain a predominantly androgen-responsive AR program, CWR22Rv1 cells exhibit a castration-resistant phenotype characterized by persistent AR signaling and expression of AR variants, including AR-V7 [Figure 8D-F]. Such differences may alter the regulatory dependence of steroidogenic pathways on the ADAM9/UBN2/AKR1C3 axis and could account for the limited modulation of UBN2 and AKR1C3 following ADAM9 silencing in CWR22Rv1 cells. However, the present data do not establish a direct causal relationship between AR isoform status and differential regulation of this axis, and further mechanistic studies will be required to define the underlying basis of this context-dependent response. Given that the present study examined a limited number of prostate cancer cell models, the observed downstream changes should be interpreted as being consistent with, rather than definitive evidence of, the proposed mechanisms. Further studies across additional prostate cancer models will be required to define the context-dependent mechanisms underlying the enhanced therapeutic response to ADAM9 targeting. Nevertheless, these results suggest that early targeting of ADAM9 may deepen AR pathway suppression and delay progression to castration-resistant disease, highlighting a potential strategy for early therapeutic intervention. These observations further demonstrate that EV-delivered siRNA can effectively modulate clinically relevant resistance pathways and enhance the therapeutic impact of existing treatment regimens.

In CRPC, where resistance mechanisms are already established, ADAM9 silencing remained effective in suppressing aggressive tumor features. EV-mediated siADAM9 delivery reduced stemness-associated programs, inhibited EMT, and suppressed extracellular matrix remodeling [Figure 7]. These findings indicate that ADAM9 contributes to tumor cell plasticity and microenvironmental adaptation, both of which are hallmarks of advanced disease. Importantly, combination treatment with EV-siADAM9 further enhanced the response to AR-targeted therapies, accompanied by upregulation of the cell cycle regulator p21, suggesting increased growth restraint and anti-tumor effects of ADAM9 silencing [Figure 8D]. ADAM9 silencing was also associated with increased expression of the cell cycle regulator p21 in both LNCaP and CWR22Rv1 cells, suggesting a cell cycle-related response to ADAM9 suppression. This response may contribute to the growth-suppressive effects of ADAM9 silencing across different androgen-response contexts. These findings position ADAM9 as an upstream regulator within a broader network of adaptive resistance mechanisms, in which tumor cells restore AR signaling through intracrine steroidogenesis and compensatory pathways, suggesting that ADAM9 targeting may complement existing therapeutic strategies aimed at suppressing AR reactivation.

Recent advances in PSMA-targeted EV engineering have demonstrated promising strategies for prostate cancer therapy, initially through peptide-guided delivery systems[24]. More recently, PSMA^{scFv}-engineered EV platforms have been developed to enable receptor-specific targeting and functional cargo delivery. Notably, Gao and colleagues reported a PSMA^{scFv}-engineered EV system loaded with N-terminal gasdermin D (GSDMD), which induced pyroptosis and remodeled the tumor microenvironment toward an immunogenic "hot" state *in vivo*[13]. While these studies collectively highlight the feasibility of PSMA-directed EV targeting, they primarily emphasize cytotoxic or immunostimulatory mechanisms. In contrast, our study advances a distinct mechanistic and translational framework by focusing on RNA interference-mediated suppression of ADAM9, a key regulator of prostate cancer progression, stemness, and therapeutic resistance. Unlike pyroptosis-based strategies that induce acute inflammatory cell death[25], our approach enables targeted modulation of oncogenic signaling networks, offering a potentially more controlled and durable therapeutic effect across both hormone-sensitive and castration-resistant contexts. Furthermore, whereas prior studies commonly utilize HEK293T-derived EV systems and protein-based cargos, our platform leverages MSC-derived EVs with intrinsic biocompatibility and clinical scalability, coupled with efficient siRNA encapsulation and delivery. The use of immortalized MSC producer cells further enhances the translational potential of this approach by providing a renewable and standardized EV source, thereby reducing donor-dependent variability and supporting consistent large-scale manufacturing. Importantly, our work extends beyond delivery validation by demonstrating functional suppression of tumor cell proliferation, migration, and stemness-associated phenotypes, thereby establishing a mechanism-driven precision therapeutic strategy.

Although PSMA-scFv functionalization enhanced EV binding and uptake in PSMA-expressing prostate cancer cells, basal binding and uptake remained detectable in PSMA-negative cells and were comparable to those of control MSC-EVs. This likely reflects, at least in part, the intrinsic tumor-cell tropism of MSC-derived EVs inherited from their parental cells, consistent with our previous observation that MSC-EVs exhibit greater binding to cancer cells than to non-cancerous cells[26]. Previous studies have implicated interactions between tumor-associated surface/ECM molecules, including integrins, EphA2, fibronectin, osteopontin, and hyaluronan, and complementary adhesion molecules carried by MSCs and their EVs, such as integrins, CD44, tetraspanins, ICAM1, and VCAM1, in mediating MSC-tumor interactions[27]. The magnitude of basal MSC-EV association may also vary among tumor-cell backgrounds, which could account for differences in the absolute proportions of EV-positive cells observed across the prostate cancer cell lines. Thus, PSMA-scFv functionalization should be interpreted as providing an additional PSMA-dependent targeting component rather than conferring absolute PSMA-exclusive specificity. This interpretation is further supported by the reduction in EV binding following PSMA knockdown and its enhancement following ectopic PSMA expression [Figure 3]. Accordingly, the engineered EV platform preferentially targets PSMA-expressing cells while retaining the intrinsic, PSMA-independent interactions of MSC-derived EVs with tumor cells.

While the present study demonstrates the efficacy of PSMA-targeted EVs for enhanced prostate cancer-specific delivery, this approach may be less effective in PSMA-low or PSMA-negative subtypes, including neuroendocrine prostate cancer, which often arises through trans-differentiation from prostate adenocarcinoma and is associated with resistance to conventional therapies[28]. However, the modular nature of the EV engineering strategy described here provides opportunities to extend this platform beyond PSMA-expressing tumors. To broaden the applicability of this platform, future studies may incorporate alternative targeting ligands directed against other prostate cancer-associated surface markers. Several candidates, including STEAP1, TROP2, CD46, Nectin-4, tissue factor, B7-H3, and DLL3, have emerged as clinically relevant targets and are currently being evaluated in antibody-based therapeutic strategies[29]. These markers may also serve as alternative targeting ligands for EV-mediated siRNA delivery in PSMA-low or

PSMA-negative disease. Targeting components of the tumor microenvironment, such as fibroblast activation protein (FAP), may further enhance delivery in heterogeneous tumor settings[30]. Importantly, the modular design of EV surface engineering enables flexible incorporation of diverse ligands, including antibody fragments, peptides, or other targeting moieties, and may support the development of multi-target or dual-targeting strategies to improve tumor coverage and therapeutic efficacy.

MSC-derived EVs are biologically active delivery vehicles that contain endogenous proteins, lipids, and nucleic acids capable of modulating recipient-cell behavior. In the present study, however, parental EVs, LAMP2B-engineered EVs, unloaded EV-PSMA^{scFv}, and siNC-loaded EV-PSMA^{scFv} did not produce detectable tumor-suppressive effects under the conditions examined. In contrast, EV-PSMA^{scFv}-siADAM9 consistently suppressed tumor-promoting phenotypes in association with effective ADAM9 silencing [Figures 6-8]. These findings support the siADAM9 cargo as the primary contributor to the observed antitumor effects and suggest that neither the MSC-EV platform nor PSMA-scFv engineering alone accounts for these phenotypes. Nevertheless, potential contributions from endogenous MSC-EV cargo and interactions between the EV platform and siRNA-mediated effects cannot be completely excluded.

Although PSMA-dependent enhancement of EV binding and uptake and functional delivery of siADAM9 were demonstrated in prostate cancer cell models, the targeting and therapeutic effects of EV-PSMA^{scFv} were evaluated primarily *in vitro*, representing an important limitation of the present study. Accordingly, the *in vivo* biodistribution, pharmacokinetics, tumor accumulation, therapeutic efficacy, off-target effects, and systemic safety of the engineered EVs remain to be established. Building on the present proof-of-concept findings, future studies using appropriate prostate cancer xenograft and orthotopic models are warranted to determine whether PSMA functionalization enhances tumor-directed EV delivery and therapeutic efficacy *in vivo* and to evaluate the safety profile of this platform before further translational development.

Conclusion

In summary, this study establishes an *in vitro* proof-of-concept for a PSMA-targeted EV platform for the delivery of siRNA against ADAM9 and demonstrates its capacity for PSMA-dependent enhancement of EV targeting, efficient intracellular delivery, and functional suppression of tumor-promoting phenotypes in prostate cancer. By disrupting the ADAM9-UBN2-AKR1C3 signaling axis, this approach attenuates adaptive androgen biosynthesis and tumor cell plasticity across both hormone-sensitive and castration-resistant disease models. Importantly, combining EV-mediated ADAM9 silencing with androgen-targeted therapies enhances therapeutic efficacy, highlighting the potential of this strategy to overcome treatment resistance. Beyond its immediate therapeutic implications, this work demonstrates the feasibility of integrating targeted EV engineering with mechanism-driven RNA interference to modulate key oncogenic pathways. The modular design of this platform further supports its adaptability to diverse molecular targets and disease contexts. Collectively, these findings provide a foundation for the development of precision RNA-based therapeutics and support further translational advancement of EV-mediated delivery systems for prostate cancer.

DECLARATIONS

Acknowledgments

The authors acknowledge the technical support provided by the TMU Core Facility. The Graphical Abstract was created with BioRender.com [Sung, S (2026), https://BioRender.com/o9mhzed].

Authors' contributions

Conceptualization and study design: Raboshakga MO, Hsieh CL, Sung SY
Performed the experiments: Raboshakga MO
Performed data analysis and interpretation: Raboshakga MO, Do AD, Shiau GHM, Shigemura K
Drafted the manuscript: Raboshakga MO
Reviewed and edited the manuscript: Do AD, Hsieh CL, Sung SY

All authors consent to the publication of the work.

Availability of data and materials

The data supporting the findings of this study are included in the article and Supplementary Materials. Further data are available from the corresponding authors upon reasonable request.

AI and AI-assisted tools statement

During the preparation of this manuscript, the AI tools Grammarly (version 1.2.268.1900, released 2026-06-10) and ChatGPT (version GPT-5.5, released 2026-04-23) were used solely for language editing and improvement of grammar, spelling, and language clarity, without unsupervised automatic generation. These tools did not influence the study design, data collection, analysis, interpretation, or the scientific content of the work. All authors take full responsibility for the accuracy, integrity, and final content of the manuscript.

Financial support and sponsorship

This work was supported by funding from the Ministry of Science and Technology (Grant numbers: NSTC 113-2314-B-040-031-, NSTC 114-2321-B-038-005-, NSTC 114-2314-B-040-032-MY3 and NSTC 114-2320-B-040-022-) and Chung Shan Medical University Hospital (Grant number: CSH-2026-E-002-Y2).

Conflicts of interest

All authors declared that there are no conflicts of interest.

Ethical approval and consent to participate

Not applicable.

Consent for publication

Not applicable.

Copyright

© The Author(s) 2026.

Supplementary Materials

Supplementary Materials

REFERENCES

1. Hussain M, Fizazi K, Shore ND, et al. Metastatic hormone-sensitive prostate cancer and combination treatment outcomes: a review. *JAMA Oncol.* 2024;10:807-20. DOI PubMed
2. Cheng Q, Butler W, Zhou Y, et al. Pre-existing castration-resistant prostate cancer-like cells in primary prostate cancer promote resistance to hormonal therapy. *Eur Urol.* 2022;81:446-55. DOI PubMed PMC
3. Stanbrough M, Bubley GJ, Ross K, et al. Increased expression of genes converting adrenal androgens to testosterone in androgen-independent prostate cancer. *Cancer Res.* 2006;66:2815-25. DOI PubMed
4. Fritzsche FR, Jung M, Tölle A, et al. ADAM9 expression is a significant and independent prognostic marker of PSA relapse in prostate cancer. *Eur Urol.* 2008;54:1097-106. DOI PubMed
5. Sung SY, Kubo H, Shigemura K, et al. Oxidative stress induces ADAM9 protein expression in human prostate cancer cells. *Cancer Res.* 2006;66:9519-26. DOI PubMed
6. Josson S, Anderson CS, Sung SY, et al. Inhibition of ADAM9 expression induces epithelial phenotypic alterations and sensitizes human prostate cancer cells to radiation and chemotherapy. *Prostate.* 2011;71:232-40. DOI PubMed PMC
7. Le TT, Hsieh CL, Lin IH, et al. The ADAM9/UBN2/AKR1C3 axis promotes resistance to androgen-deprivation in prostate cancer. *Am J Cancer Res.* 2022;12:176-97. PubMed PMC
8. Zhang J, Chen B, Gan C, Sun H, Zhang J, Feng L. A comprehensive review of small interfering RNAs (siRNAs): mechanism, therapeutic targets, and delivery strategies for cancer therapy. *Int J Nanomedicine.* 2023;18:7605-35. DOI PubMed PMC
9. Chen H, Yao H, Chi J, et al. Engineered exosomes as drug and RNA co-delivery system: new hope for enhanced therapeutics? *Front Bioeng Biotechnol* 2023;11:1254356. DOI PubMed PMC
10. Bakht MK, Yamada Y, Ku SY, et al. Landscape of prostate-specific membrane antigen heterogeneity and regulation in AR-positive and AR-negative metastatic prostate cancer. *Nat Cancer.* 2023;4:699-715. DOI PubMed PMC

11. Tagawa ST, Milowsky MI, Morris M, et al. Phase II study of Lutetium-177-labeled anti-prostate-specific membrane antigen monoclonal antibody J591 for metastatic castration-resistant prostate cancer. *Clin Cancer Res.* 2013;19:5182-91. DOI PubMed PMC
12. Muñoz-López P, Ribas-Aparicio RM, Becerra-Báez EI, et al. Single-Chain fragment variable: recent progress in cancer diagnosis and therapy. *Cancers.* 2022;14:4206. DOI PubMed PMC
13. Gao K, Xi W, Ni J, et al. Genetically modified extracellular vesicles loaded with activated gasdermin D potentially inhibit prostate-specific membrane antigen-positive prostate carcinoma growth and enhance immunotherapy. *Biomaterials.* 2025;315:122894. DOI PubMed
14. Hung SC, Yang DM, Chang CF, et al. Immortalization without neoplastic transformation of human mesenchymal stem cells by transduction with HPV16 E6/E7 genes. *Int J Cancer.* 2004;110:313-9. DOI PubMed
15. Silver DA, Pellicer I, Fair WR, Heston WD, Cordon-Cardo C. Prostate-specific membrane antigen expression in normal and malignant human tissues. *Clin Cancer Res.* 1997;3:81-5. PubMed
16. Alvarez-Erviti L, Seow Y, Yin H, Betts C, Lakhal S, Wood MJ. Delivery of siRNA to the mouse brain by systemic injection of targeted exosomes. *Nat Biotechnol.* 2011;29:341-5. DOI PubMed
17. Welsh JA, Goberdhan DCI, O'Driscoll L, et al. ; MISEV Consortium. Minimal information for studies of extracellular vesicles (MISEV2023): from basic to advanced approaches. *J Extracell Vesicles.* 2024;13:e12404. DOI PubMed PMC
18. Horoszewicz JS, Leong SS, Chu TM, et al. The LNCaP cell line--a new model for studies on human prostatic carcinoma. *Prog Clin Biol Res.* 1980;37:115-32. PubMed
19. Dehm SM, Schmidt LJ, Heemers HV, Vessella RL, Tindall DJ. Splicing of a novel androgen receptor exon generates a constitutively active androgen receptor that mediates prostate cancer therapy resistance. *Cancer Res.* 2008;68:5469-77. DOI PubMed PMC
20. Huang F, Li K, Shevach JW, Wang Q. Emerging therapies to overcome antiandrogen resistance and beyond in lethal prostate cancer. *J Natl Cancer Cent.* 2026;6:42-57. DOI PubMed PMC
21. Hu B, Zhong L, Weng Y, et al. Therapeutic siRNA: state of the art. *Signal Transduct Target Ther.* 2020;5:101. DOI PubMed PMC
22. Kwok ZH, Wang C, Jin Y. Extracellular vesicle transportation and uptake by recipient cells: a critical process to regulate human diseases. *Processes.* 2021;9:273. DOI PubMed PMC
23. Rajasekaran SA, Anilkumar G, Oshima E, et al. A novel cytoplasmic tail MXXXL motif mediates the internalization of prostate-specific membrane antigen. *Mol Biol Cell.* 2003;14:4835-45. DOI PubMed PMC
24. Severic M, Ma G, Pereira SGT, Ruiz A, Cheung CCL, Al-Jamal WT. Genetically-engineered anti-PSMA exosome mimetics targeting advanced prostate cancer *in vitro* and *in vivo*. *J Control Release.* 2021;330:101-10. DOI PubMed
25. Yu P, Zhang X, Liu N, Tang L, Peng C, Chen X. Pyroptosis: mechanisms and diseases. *Signal Transduct Target Ther.* 2021;6:128. DOI PubMed PMC
26. Do AD, Chu SS, Giang LH, et al. Delivery of LOXL1-AS1-siRNAs using targeting peptide-engineered extracellular vesicles with focused ultrasound to suppress medulloblastoma metastasis. *J Nanobiotechnology.* 2025;23:460. DOI PubMed PMC
27. Rahimi Tesiye M, Abrishami Kia Z, Rajabi-Maham H. Mesenchymal stem cells and prostate cancer: a concise review of therapeutic potentials and biological aspects. *Stem Cell Res.* 2022;63:102864. DOI PubMed
28. Bakht MK, Derecichei I, Li Y, et al. Neuroendocrine differentiation of prostate cancer leads to PSMA suppression. *Endocr Relat Cancer.* 2018;26:131-46. DOI PubMed
29. Ozay ZI, Hage Chehade C, Gebrael G, et al. Antibody-drug conjugates in prostate cancer: current landscape and future directions. *Ther Adv Med Oncol.* 2026;18:17588359261424672. DOI PubMed PMC
30. Brennen WN, Isaacs JT, Denmeade SR. Rationale behind targeting fibroblast activation protein-expressing carcinoma-associated fibroblasts as a novel chemotherapeutic strategy. *Mol Cancer Ther.* 2012;11:257-66. DOI PubMed PMC

Disclaimer/Publisher's Note: All statements, opinions, and data contained in this publication are solely those of the individual author(s) and contributor(s) and do not necessarily reflect those of OAE and/or the editor(s). OAE and/or the editor(s) disclaim any responsibility for harm to persons or property resulting from the use of any ideas, methods, instructions, or products mentioned in the content.

© The Author(s) 2026. Open Access This article is licensed under a Creative Commons Attribution 4.0 International License (https://creativecommons.org/licenses/by/4.0/), which permits unrestricted use, sharing, adaptation, distribution and reproduction in any medium or format, for any purpose, even commercially, as long as you give appropriate credit to the original author(s) and the source, provide a link to the Creative Commons license, and indicate if changes were made.